Additive manufacturing-based repair of IN718 superalloy and high-cycle fatigue assessment of the joint

Sarkar, R., Chen, B., Fitzpatrick, M. E., Fabijanic, D. & Hilditch, T

Original citation & hyperlink:

Sarkar, R, Chen, B, Fitzpatrick, ME, Fabijanic, D & Hilditch, T 2022, 'Additive manufacturing-based repair of IN718 superalloy and high-cycle fatigue assessment of the joint', Additive Manufacturing, vol. 60, no. Part A, 103276.
https://doi.org/10.1016/j.addma.2022.103276

DOI 10.1016/j.addma.2022.103276
ISSN 2214-7810
ESSN 2214-8604

Publisher: Elsevier

Additive manufacturing-based repair of IN718 superalloy and high-cycle fatigue assessment of the joint

Riddhi Sarkar[a,c,*], Bo Chen[b], Michael E.Fitzpatrick[c], Daniel Fabijanic[a], Tim Hilditch[d]

[a] Institute for Frontier Materials, Deakin University, Waurn Ponds, Victoria 3216, Australia
[b]School of Engineering, University of Leicester, Leicester LE1 7RH, UK
[c]The Institute for Future Transport and Cities, Coventry University, Coventry CV1 5FB, UK
[d]School of Engineering, Deakin University Waurn Ponds, Victoria 3216, Australia

Abstract

Room-temperature high-cycle fatigue (HCF) of IN718 repaired joint via laser direct energy deposition (DED) were studied with the fatigue axis perpendicular to the joint interface. Solution treated and aged (STA) were compared with directly aged (DA) conditions. The wrought IN718 substrate showed equiaxed grains with a size of ~90 μm and a high fraction of annealing twins, whereas the DED deposit revealed a mixture of equiaxed and columnar grains with an average size of ~20 μm. There was little difference between the STA and DA conditions in the grain length-scale. Micro-hardness results highlighted the need for the heat treatment as it can remove the heat-affected zone and hardness dip, creating a uniform hardness profile across the joint. Although the monolithic DED deposit had a similar tensile strength to the wrought substrate, the DED joint exhibited an overall decreased HCF performance, regardless of the heat treatment conditions. When the fatigue stress was low, the STA condition had a better HCF performance than the DA, however, the opposite trend appeared for the high stress, resulting in a cross-over point on the stress-life *S-N* plot. Interrupted fatigue tests, combined with microscopy and fractography, revealed that the fatigue failure occurred in the substrate for the DED joint in the DA condition, whilst in the deposit zone for the STA condition due to the distribution and fracture of the Laves and δ phases. Grain boundary cracking in the substrate near the substrate-to-deposit interface can occur in both cases, probably due to the Nb-rich liquid ilms.

Keywords: Additive Manufacturing, Direct Energy Deposition, Inconel 718, Microstructure, High Cycle Fatigue.

1. Introduction

Inconel 718 (IN718) Ni-base superalloy with good mechanical strength at high temperature and resistance to oxidation finds its industrial applications in jet engine parts, gas turbines, and various components in fossil fuel and nuclear power plants [1–3]. Mechanical properties, especially tensile properties of IN718 fabricated using various additive manufacturing (AM) methods, were reported in the literature [4–8]. In general, the tensile strength of AM IN718 parts in as-deposited conditions was significantly lower than the wrought IN718. However, post-processing heat treatments resulted in a strength level comparable to the wrought material due to the formation of γ' and γ'' precipitates. Despite the strength enhancement achieved by using either the direct ageing (DA) or solution treating and ageing (STA), the ductility of the AM IN718 in the DA condition was inferior compared to the STA condition and the wrought IN718, owing to the presence of Laves phase associated with the non-equilibrium solidification during the AM process [5,8–10].

High-cycle fatigue (HCF) is one of the important failure mechanisms [11,12]. The fatigue properties of wrought IN718 are often linked to the δ-phase, although its effect is not always consistent. It was reported by An et al. [13] that the δ-phase caused the fatigue performance deterioration. However, Li et al. [14] found improved resistance to intergranular fatigue cracks due to the presence of the δ-phase at grain boundaries. The highly complex thermal history during AM leads to significant microstructural variations, including the grain size, secondary phase and defect, that can affect the fatigue performance [15–20]. Gribbin et al. [15] observed that wrought IN718 exhibited better HCF performance than the AM IN718 in the STA condition because of the porosities and δ-phase precipitates in the latter. Sui et al. [11] found improved HCF performance of wrought IN718 compared to laser AM IN718 in a DA condition, which was attributed to the presence of δ-phase in the wrought samples. The Laves phase fragmented at high-stress levels, creating microvoids in the Laves-matrix interface, which led to the early crack initiation and hence the poor fatigue life [11,21]. However, at lower stress amplitudes, improved fatigue life was observed in the AM material that was attributed to the Laves phase hindering the crack propagation. Amsterdam et al. [19] investigated the HCF properties of IN718 processed by laser direct energy deposition (DED) and found the fatigue performance comparable to the wrought, even with the presence of porosities (size of 2 μm to 100 μm, with the majority being less than 25 μm) in the DED IN718.

A significant potential for AM applications is component repair, especially for the DED, a blown-powder AM process. Fusion welding repair of IN718 was studied previously [22–24], revealing two primary cracking mechanisms of the micro-fissuring and heat-affected zone cracking [25–27]. To the best of the authors' knowledge, there has been no attempt to assess the HCF performance of the DED repaired joint and literature concerning the fatigue of IN718 repairs is exclusively limited to fusion welding.

Ono et al. [28] found that the HCF strength of an electron beam welded IN718 joint was lower than the base metal, with cracks occurring in the heat-affected zone. The fatigue crack initiation was attributed to the NbC, Laves and δ phases. Sivaprasad and Raman [29] studied the HCF performance of IN718 weldments in DA and STA conditions and observed irregular-shaped transgranular fatigue crack growth, causing the failure in the weld zone. The failure occurred predominantly through the Laves phase in the DA condition, whilst in the region around the δ and Laves phases in the STA condition. Their subsequent work [30] observed that the increased volume fraction of Laves phase resulted in the fatigue-life reduction. The STA condition exhibited better fatigue performance at low-stress levels, however, the DA condition performed better than the STA counterpart under high-stress levels. For the STA condition, the δ-needles affected the fatigue life more adversely than the Laves phase [30]. Alexopoulos et al. [31] found a greater decrease in fatigue performance at the higher stress than the lower stress by comparison of the TIG-welded with the wrought IN718.

To summarise, there is a contrasting viewpoint about the HCF performance of AM IN718 when compared to the wrought material, especially due to the complex microstructure formed under the non-equilibrium solidification, which can trigger some solid-phase transformation during the post-processing heat treatment. In addition, the HCF performance of the AM repaired joint structure has not received much attention in the literature. The present work studies the room temperature HCF performance and failure mechanisms of DED IN718 in both the DA and STA conditions. Our focus is primarily on the DED repaired joint with the fatigue loading axis being perpendicular to the joint interface. In addition to the fatigue to failure, interrupted fatigue tests have been designed to elucidate the role of various microstructural constituents on the initiation and propagation of fatigue cracks.

2. Experimental

2.1. Sample fabrication

Plasma atomised IN718 powders were obtained from GE additive with a size range from 45 µm – 105 µm, having a spherical shape as shown in Fig 1. An Optomec LENS MR-7 apparatus was used for the DED repair as well as the bulk sample build, with the laser power of 500 W and spot size of 1.2 mm, scanning speed of 6.3 mm/s, and powder flow rate of 12 g/min. The layer thickness was 0.48 mm, and the hatch spacing was 0.95 mm. The melt pool overlap was estimated as ~50%. As schematically shown in Figure 2(a), an alternate scanning pattern was used. The oxygen concentration of the build chamber was maintained at less than 3 ppm during the deposition. Argon was used as the shielding gas and carrier gas with a flow rate of 15 l/min and 6 l/min, respectively. Wrought IN718 with dimensions of 50 mm × 20 mm × 40 mm (length × width × height) were used as the substrate for the DED repairs. This essentially created three characteristic regions: the DED IN718 deposit, wrought IN718 substrate plate and the substrate-to-deposit interface.

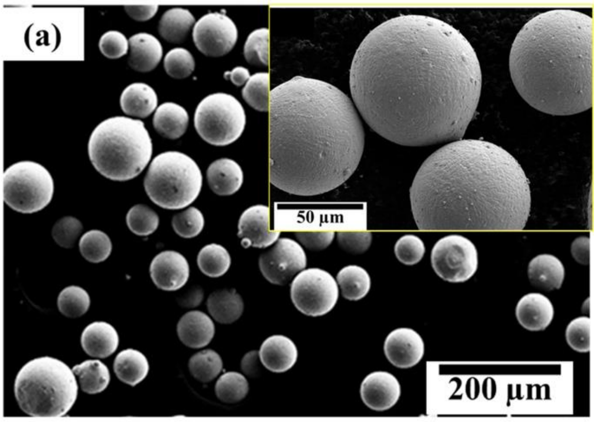

Fig 1: SEM images of the feedstock IN718 powders.

Schematics of the sample preparation for fatigue tests are shown in Fig 2a and Fig 2b. Repair region with similar dimensions to the wrought substrate plate was deposited, followed by using electro-discharge machining to make the hourglass HCF samples, according to ASTM E466 [32]. The HCF samples consisted of 50% wrought substrate and 50% DED deposit with the substrate-to-deposit interface in the narrowest part, Fig 2b. This hourglass sample geometry ensured the maximum cyclic stress was applied at the region as close as possible to the joint interface. After the fatigue sample extraction, some HCF specimens were subjected to solution heat treatment followed by ageing, abbreviated as STA, while the other received a direct ageing, abbreviated as DA. The solution treatment was performed at 980 °C for 1 h, followed by water quenching. The ageing treatment involved heating at 720 °C for 8 h, followed by furnace cooling at a rate of 55 °C/h to 620 °C, and then thermal soaking at 620 °C for 8 h, and finally air cooling to room temperature. Previous work on selective laser melted (SLM) IN718 showed that solution treatment at 1100 °C caused significant grain growth, despite a complete dissolution of Laves phase [5]. Thus, the solution treatment temperature in the present work was chosen to be 980 °C. In addition, both the STA and DA heat treatment parameters conform with those adopted for the cast and wrought IN718 [5,10,33].

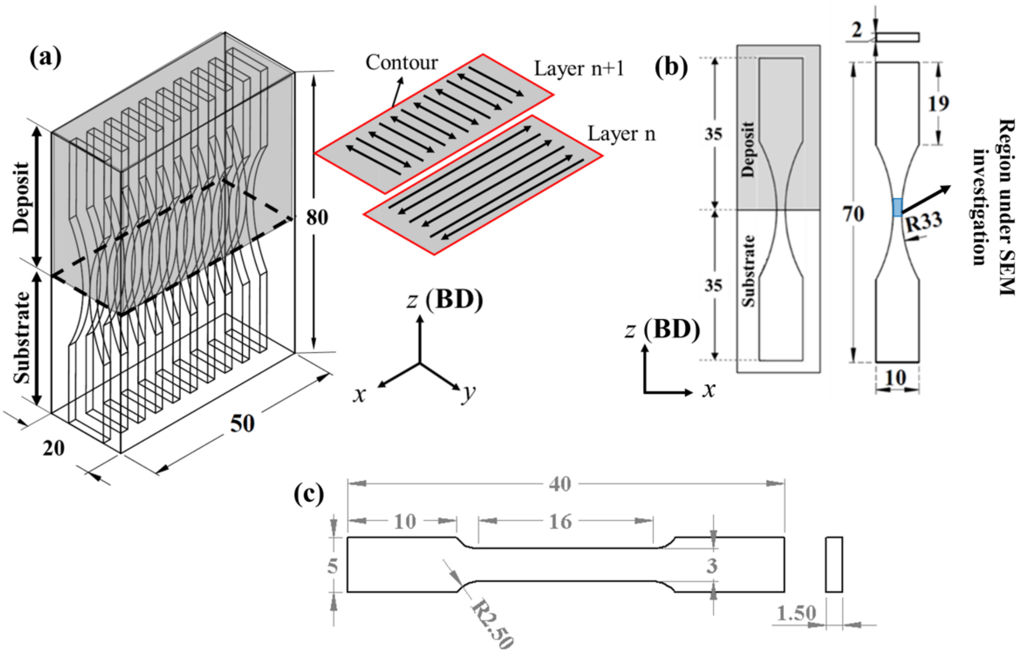

Fig 2: Schematics of (a) laser DED repaired block; (b) hourglass fatigue samples extracted from the block; (c) samples for tensile testing.

2.2. Monotonic and fatigue testing

Vickers hardness of the repaired IN718 was measured using a Struers Microhardness tester with a load of 500 gf and a dwell time of 15 sec. To understand the spatial variation in hardness, indentations were performed with a spacing of 200 µm covering three characteristic regions of the deposit, the substrate-to-deposit interface and the substrate.

Tensile tests were conducted on the wrought IN718 in the STA condition and on the DED IN718 in both the DA and STA conditions. The process parameters used to build the DED IN718 sample block were identical to those employed for the DED repair. The tensile specimens (Fig 2c) were machined according to ASTM E8 [34], and all tests were carried out at room temperature on a ±100-kN-capacity hydraulic machine with a constant crosshead speed corresponding to a nominal strain rate of 10^{-3} s^{-1}. The tensile results formed an important basis to choose the fatigue stress levels.

Fatigue tests were carried out at room temperature for generating the stress-life (*S*-*N*) curve, using Instron E10000 with a ±10-kN load cell. Stress-controlled fatigue tests were performed using a sinusoidal waveform at R = 0.1 and a frequency of 50 Hz. No bending or buckling was observed during the specimen fixing and fatigue testing. Prior to fatigue testing, specimen surfaces were mechanically ground using emery papers successively from 240 Grit to 4000 Grit.

After the establishment of the *S-N* curve for the DED IN718 repair joint, the initiation and growth behaviour of fatigue cracks was studied in detail by adopting the single-specimen and interrupted testing procedure. The stochastic nature of fatigue leads to a large specimen-to-specimen variation (e.g. fatigue life). Thus, any post-mortem examination to trace the fatigue crack behaviour needs to be based on a large number of tests, e.g. [35]. In contrast, performing the single-specimen and interrupted testing approach bypasses the stochastic nature to some extent, as it permits us to monitor the crack development from various possible sources and assessing the role of microstructure over various stages towards the anticipated fatigue life. Prior to the test, specimens were further polished with diamond suspensions from 3 µm to 1 µm and then with OPS colloidal silica suspension. These interrupted experiments were conducted at two stress levels: one at maximum cyclic stress of $\sigma_{\max}$ = 650 MPa while the other at $\sigma_{\max}$ = 428 MPa. The test procedure consisted of three steps: (i) cyclically loading the specimen at a target stress level to the predefined cycle before the actuator movement was arrested for allowing load relaxation and specimen removal from the test machine; (ii) the cyclically loaded specimen was ultrasonically cleaned and subsequently examined using scanning electron microscopy (SEM); (iii) the specimen was remounted in the machine and fatigue loaded at the same target stress levels for the next set of cycles until re-examination in the SEM or test end. The test was interrupted at various fatigue cycles ranging from 10 pct to 90 pct of the anticipated fatigue life N_f as determined by the uninterrupted test.

2.3. Microstructural characterisation and fractography

Metallographic samples were sectioned from the middle part across the repaired joint as shown in Fig 2b. They were mechanically ground successively from 240 Grit to 4000 Grit, polished with diamond suspension from 3 µm to 1 µm and finally with OPS colloidal silica suspension. A Supra VP55 FEG-SEM, equipped with a backscattered electron (BSE) detector, was used for imaging. Energy dispersive X-ray spectroscopy (EDS) was used to aid the phase identification. An electron backscatter diffraction (EBSD) system from Oxford Instrument was employed to measure the texture and grain size. EBSD data were collected with a step size of 2.5 µm and analysed with HKL Channel 5 software. The circle equivalent diameter generated by the HKL software from the EBSD data was used for the grain size measurements. The 60° <111> twin boundary was not considered during grain reconstruction.

For the interrupted fatigue specimens, a surface area of approximately 2 × 2 mm^2 in the centre of the flat hourglass specimen was tracked and examined using the SEM. The total crack length and number density of microcracks were then calculated as the average number of cracks per unit area in mm^2; a similar approach was adopted by Majumdar et al. [36] to examine fatigue crack initiation and propagation on IF steel sheets and Peng et al. [37] on another AM Ni-base superalloy. The SEM fractography and the cross-section surface observation were conducted to determine the fatigue failure mechanism.

3. Results

3.1. DED repaired microstructure

The chosen DED parameter set resulted in highly dense deposits with a porosity level of <0.05%. No other defects were observed in the heat-affected zone of the wrought substrate IN718 or at the deposit-to-substrate interface. For both the DA and STA conditions, the substrate region had equiaxed grains with an average grain size of ~90 µm, Fig 3a and Fig 3b. In addition, a high fraction (>50%) of ∑3 <110> of twin boundaries was identified, as manifested by a clear misorientation peak at 60°±5° on the misorientation distribution plot, Fig 3c for DA while Fig 3d for STA conditions. On the contrary, the deposit zone exhibited a heterogeneous distribution of columnar and equiaxed grains along the Z build direction with a high fraction of low-angle grain boundaries (defined by the misorientation angle of 2º to 10º). For the DA condition, the grain size in the deposit zone was measured to be 18.5±0.3 µm, while that in the substrate was 91.9±11.4 µm. For the STA condition, the grain size was found to be 20.5±0.5 µm in the deposit zone and 88.3±9.8 µm in the substrate. The smaller grain size as measured in the deposit zone is a combined effect of smaller-sized equiaxed grains and fine columnar grains (with a high height-to-width ratio).

The inverse pole figure (IPF) maps for both the DA and STA conditions revealed a relatively weak crystallographic texture along {001} || build direction, with the maximum multiple of uniform density (MUD) value of 2.54 for the DA while 3.34 for the STA condition as determined from the pole figures, Fig 3e and Fig 3f. Both pole figures were based on >4000 grains; hence, the texture interpretation has the required statistical importance. Moreover, analysing the columnar grains alone in the deposit zone (containing >3000 grains) resulted in the maximum MUD value of 2.98 and 3.08 for the DA and STA conditions, respectively. This indicates that there is no preferential texture in the deposit zone. Therefore, the effect of texture on fatigue behaviour is judged to be limited.

Additional EBSD scan was performed on the as-deposited condition of the DED repaired joint (i.e. receiving no post-processing heat treatment), with the orientation map presented in Fig 3g and the corresponding pole figure in the figure inset. In the as-deposited condition, the average grain size in the deposit zone was measured to be 19.03±0.3 μm, Fig 3h, and the grain size distribution histogram is similar to the DA and STA conditions. In addition, the maximum MUD was determined as 3.79, which is similar to that of the DA and STA conditions. Thus, the grain morphology in the deposit zone remained unchanged after the post-processing heat treatment.

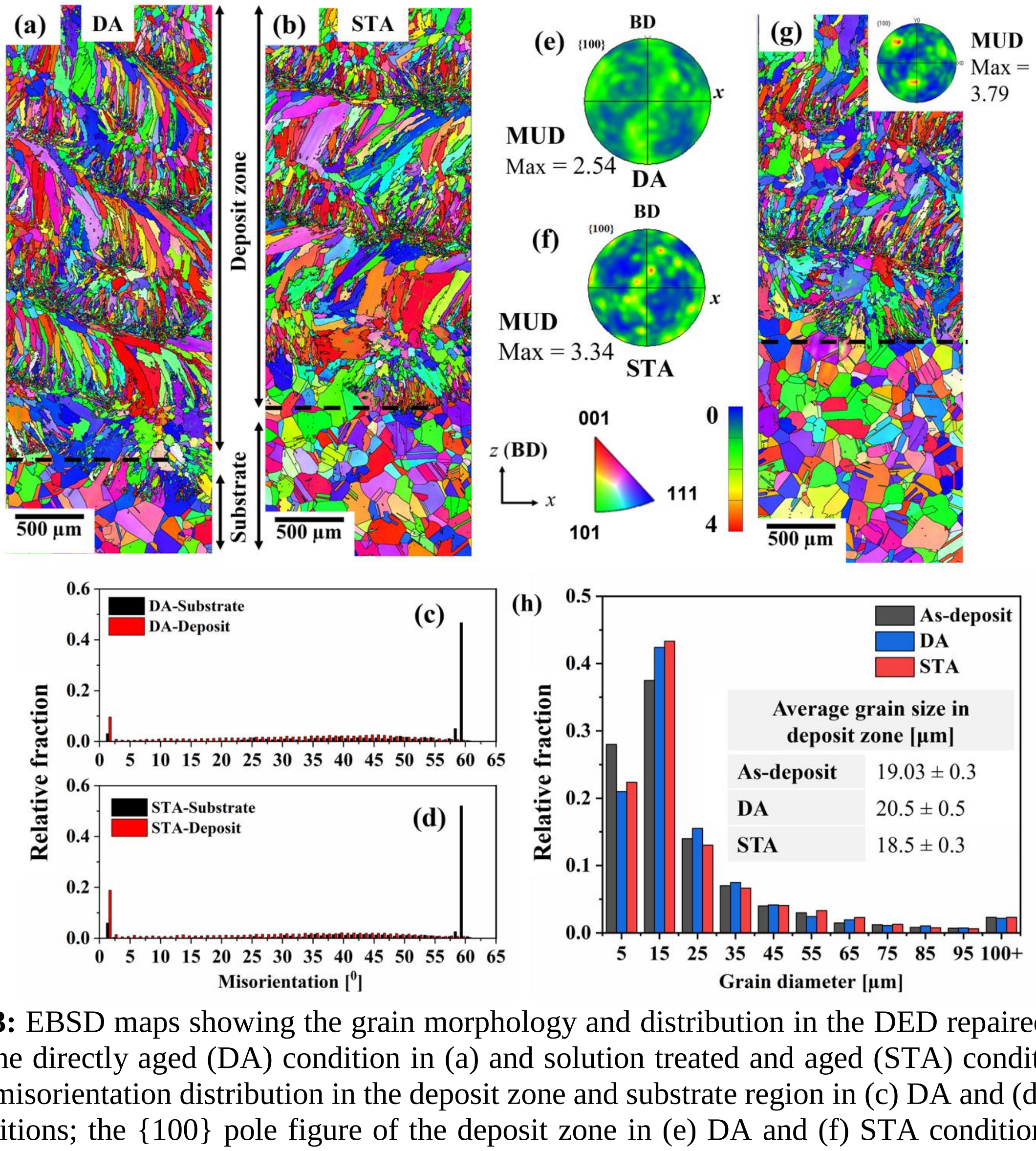

Fig 3: EBSD maps showing the grain morphology and distribution in the DED repaired joint for the directly aged (DA) condition in (a) and solution treated and aged (STA) condition in (b); misorientation distribution in the deposit zone and substrate region in (c) DA and (d) STA conditions; the {100} pole figure of the deposit zone in (e) DA and (f) STA conditions; (g) EBSD orientation map and {100} pole figure from the DED repaired joint in as-deposited condition; (h) comparison of the grain size distribution for the as-deposited, DA and STA conditions as measured from the deposit zone.

Fig 4a shows an SEM micrograph of the wrought substrate IN718 in STA condition exhibiting near-equiaxed grains with twins in the γ-matrix, while the inset shows the presence of blocky MC particles and dispersed δ-phase precipitates along the grain boundaries. The micro-hardness was measured to be 425±20 Hv, which is similar to previous work [38]. Fig 4b shows the EDS line scan analysis confirming the presence of (Nb, Ti) C in the wrought IN718. The NbC appears as a brighter blocky carbide and TiC as a darker round-shaped one.

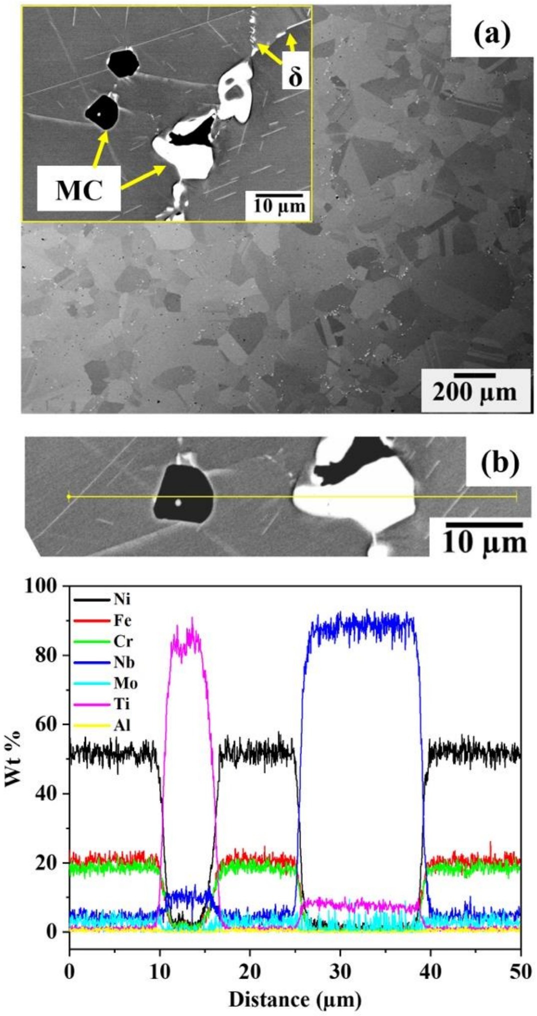

Fig 4: Wrought IN718 substrate: (a) BSE-SEM micrograph showing near-equiaxed grains, and the figure inset showing blocky carbides and δ phases on the grain boundaries; (b) EDS line scan for identification of NbC and TiC.

Fig 5a shows the SEM overview of the DED IN718 joint in the DA condition, containing the substrate and DED deposited material with the black dashed lines indicating their interface. Fig 5b and Fig 5c show the high-magnification micrographs of the substrate and deposit zone, respectively. The brighter contrast particles appearing on both micrographs were confirmed by EDS point analysis as the Laves phase containing higher than 14 wt.% of Nb.

For the substrate, Laves phase was observed mainly at or near the grain boundaries, Fig 5b. By comparison, a higher volume fraction of Laves phase appeared in the DED deposit region, which could be due to the grain sub-structure, inducing many low-angle grain boundaries, as revealed by our EBSD-based misorientation analysis in Fig. 3c. Laves phase in the deposit zone formed in the inter-dendritic regions is as expected, due to the elemental partitioning of Nb and Mo during the non-equilibrium solidification condition of the DED process [10,39]. Fig 5d shows the corresponding EDS elemental map, where the Nb-rich grain boundaries can be seen in the substrate near the deposit-to-substrate interface. These Nb-rich grain boundaries were likely induced by the constitutional liquation of NbC carbides. The temperature experienced by the substrate near the interface should be high enough to induce liquation of carbides (1200 ºC to 1250 ºC). The constitutional liquefication of the NbC can result in the formation of Nb-rich liquid film at the boundaries and then solidifies in Laves phase composition [26,40].

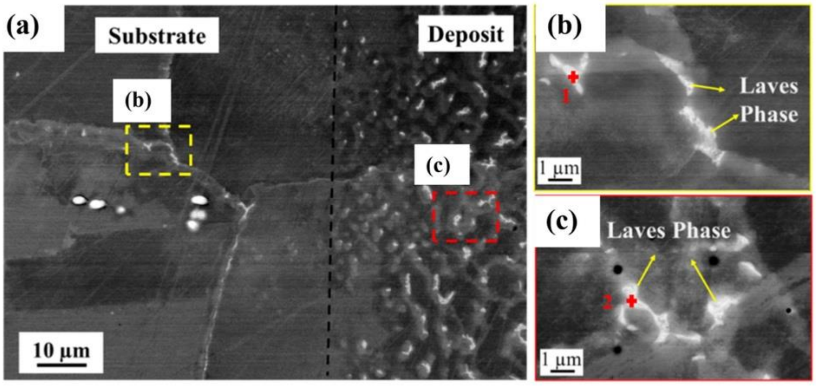

Spectrum	Composition (Wt%)							
	Ni	Cr	Fe	Nb	Mo	Ti	Al	Phase
Spectrum 1	44.6	14.8	14.7	19.6	4.6	1.6	0.3	Laves
Spectrum 2	48.0	16.1	15.5	14.4	4.0	1.5	0.5	Laves

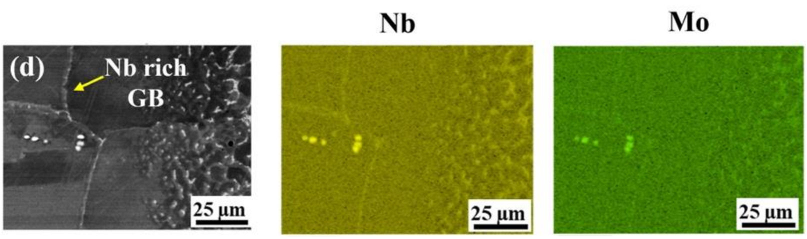

Fig 5: Microstructure of the DED IN718 joint in DA condition: (a) SEM micrograph of the deposit-to-substrate region; (b) and (c) high-magnification view showing the phases in the substrate and deposit zone, respectively; (d) EDS map showing Nb and Mo segregation on the substrate grain boundary. The marked points 1 and 2 in (b) and (c) indicate EDS point analysis with the results given in the table.

Fig 6a shows the overview microstructure of the DED IN718 joint in the STA condition, where the deposit region is on the left, while that of the wrought substrate is on the right. Representative SEM micrographs at higher magnification for the deposit region is shown in Fig 6b, while that of the substrate region is shown in Fig 6c. The STA heat treatment resulted in the formation of δ precipitates in both the deposit zone (Fig 6b) and substrate (Fig 6c). The δ phase can be easily identified by its needle-like shape, and its precipitation occurred exclusively around Laves particles. The δ phase is an orthorhombic Ni_3Nb precipitate, with Nb concentration of 8 – 10 wt % [10], which precipitates in the range of 860 ºC to 995 ºC (e.g. [41–43]). Qi et al. [10] claimed that high cooling rates during the repair process restricted the formation of the δ phase in as-deposited IN718, and the low heating rates during the subsequent solution treatment at 980ºC resulted in precipitation of the δ phase by dissolving the Laves phase. As a result, in the deposit zone, the δ precipitates are expected to form along the inter-dendritic region around the Laves phases. Moreover, the solidification conditions during the repair/deposition process resulted in a heterogeneous distribution of δ precipitates in the deposit zone. In the substrate, δ precipitates were observed close to the grain boundaries (Fig 6c). Like the observation in the DA condition, the presence of Nb-rich liquid film (with Laves phase composition) along the grain boundaries can still be seen in the substrate close to the deposit-to-substrate interface, Fig 6d and the companion table. This indicates a higher temperature than 980ºC would be required to dissolve the liquid film completely. To summarise, the primary microstructure difference between the STA and DA conditions is the presence of δ precipitates (that are formed along with Laves phase) in the inter-dendritic region of the DED deposit zone and along grain boundaries in the substrate near the deposit-to-substrate interface.

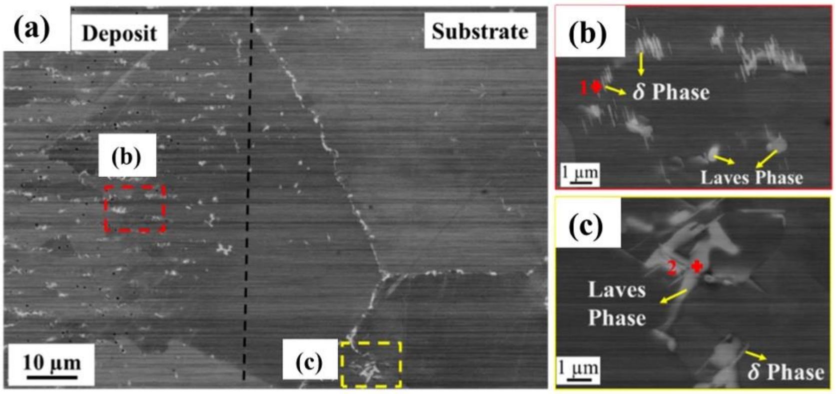

Spectrum	Composition (Wt%)							
	Ni	Cr	Fe	Nb	Mo	Ti	Al	Phase
Spectrum 1	49.6	16.2	15.9	11.5	5.2	1.2	0.4	δ phase
Spectrum 2	40.7	16.0	17.8	16.7	7.9	0.8	0.2	Laves

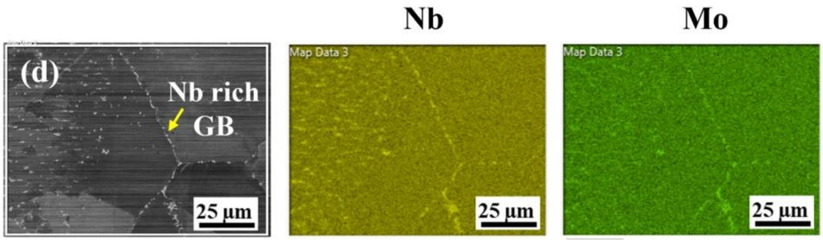

Fig 6: Microstructure of the DED IN718 joint in STA condition: (b) and (c) the enlarged view showing the phases in the substrate and deposit zone, respectively; (d) EDS map showing Nb, and Mo segregation on the substrate grain boundary. The marked points 1 and 2 in (b) and (c) indicate EDS point analysis with the results given in the table.

The hardness profile across the deposit-to-substrate interface is shown in Fig 7a. In the as-deposited condition (i.e. receiving no heat treatment), the hardness in the deposit zone was considerably lower (~250 Hv) compared to the hardness in the substrate (450 Hv). The high cooling rates of the DED process did not allow the formation of γ′ and γ″ precipitates [38], which resulted in the low hardness in the deposit zone. A heat-affected zone with ~500 μm in width can be seen at the substrate side near the deposit-to-substrate interface, Fig 7a, and this region was characterised by a dip in hardness values. A similar observation was reported in DED processed IN718 by Zhai et al. [38]. It is likely that high temperatures during the DED repair already triggered the dissolution of the δ phase in the substrate (1269 K to 1288 K for δ-solvus temperature range) [2,44], and thereby led to a decreased hardness value. The heat-affected zone seemed to extend up to approximately 800 μm away from the deposit-to-substrate interface so that the hardness in the substrate wrought IN718 was restored to the expected high value. Fig 7a also reveals that a uniform hardness was obtained across the joint in both the STA and DA conditions, which can be attributed to the formation of the γ′ and γ″ precipitates. Attempt was made to confirm the presence of γ′ and γ″ precipitates in the heat-treated condition of DED IN718. Metallography sample preparation involved polishing down to 1 µm diamond suspension, and then chemical etching in a solution of 1.5 g $CuSO_4$ + 20 mL HCl + 10 mL ethanol. Under the SEM scrutiny (Fig 7b), the phase contrast seems to suggest the nanometre scaled γ′ and γ″ precipitates with the size of ~15 nm, which certainly reaches the limit of SEM resolution. Future work is needed to reveal these precipitates more clearly using transmission electron microscopy, which is beyond the scope of the present work.

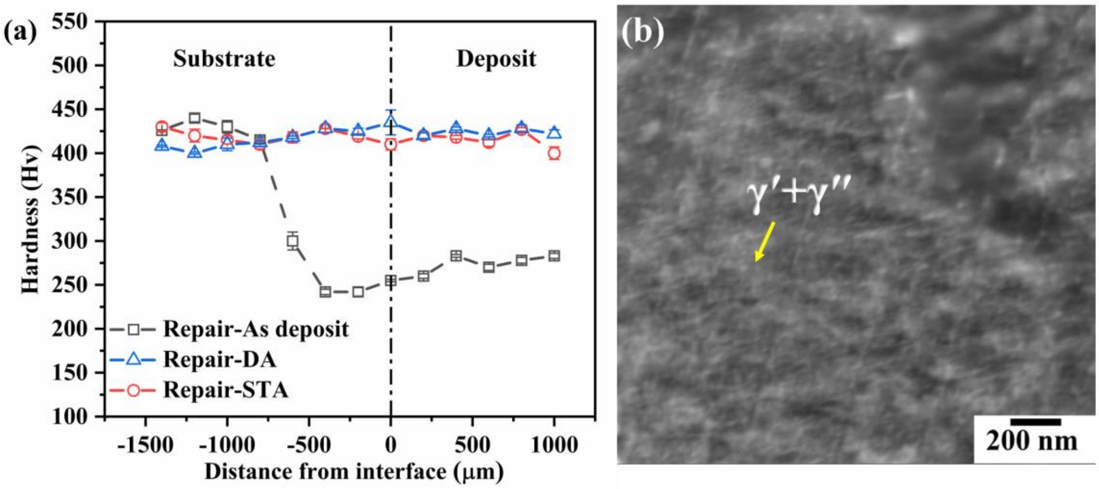

Fig 7: (a) Hardness variation in the DED repaired joint across the deposit-to-substrate interface in the as-deposited, STA and DA conditions; (b) a representative SEM micrograph showing the chemically etched DED IN718 in the deposit zone in the DA condition

3.2. Tensile properties

Fig 8 shows the engineering stress-strain response of the substrate in STA condition and DED IN718 in the DA and STA conditions. The derived tensile properties are summarised in Table 1. The yield strength, tensile strength, and elongation-to-failure (expressed as a percentage) agree fairly well with the values of DED IN718, tested under similar heat-treated conditions [10,38]. The tensile ductility for the DA sample of the DED IN718 was significantly low of ~8%, compared to ~17% of the STA sample and ~22% for the wrought IN718 in the STA condition. The brittle Laves phase provides an easy path for crack formation and failure, which seems to be responsible for the low tensile ductility in the DA sample. By contrast, the improved ductility in the STA condition can be attributed to the formation of δ precipitates as a result of partial dissolution of the Laves phase. The yield strength of the DED IN718 in DA and STA conditions were slightly higher than the wrought substrate, with the measured difference in yield strength being <5%. Therefore, the yield strength of the wrought substrate was used to choose the appropriate stress levels for the HCF testing, i.e. maximum cyclic stress levels ranged from 35% to 90% of the yield strength.

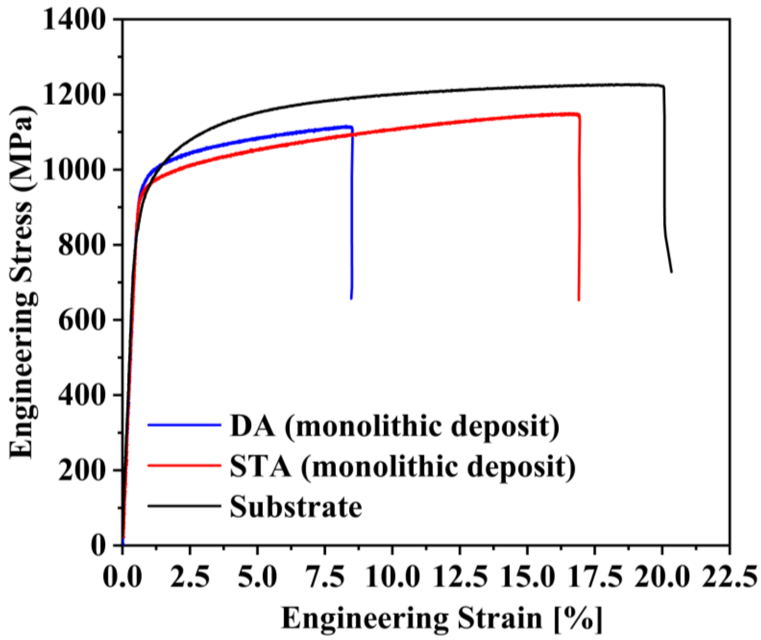

Fig 8: Tensile stress-strain curves measured using the tensile specimen as per Fig 2c.

Table 1: Tensile properties of IN718 of the wrought substrate as well as the DED build in both the STA and DA conditions. Note: the tensile axis was parallel to the Z-build direction, and at least three tests per condition was conducted to obtain the average value.

Tensile properties of IN718	Heat treated condition		
	IN718 – DA	IN718 – STA	Wrought – STA
Elastic modulus [GPa]	194 ± 17	173 ± 10	176 ± 10
$\sigma_{YS(0.2)}$ [MPa]	948 ± 13	946 ± 20	924 ± 12
σ_{UTS} [MPa]	1134 ± 16	1134 ± 18	1226 ± 10
Elongation [%]	8.50 ± 0.2	17.20 ± 3.5	22.4 ± 0.6

3.3. Fatigue *S-N* curves

The *S-N* curves of the DED repaired joint (STA and DA conditions) in comparison with the wrought IN718 (STA condition) are presented in Fig 9. Fatigue run-out was defined as the test which did not fail after 5×10^6 cycles, and these data points were marked with the right arrow. The fatigue cycles of 5×10^6, as opposed to 10^7, has been chosen as the fatigue run-out in the present work to maintain consistency with a previous work on SLM IN718 [45]. One sample (the repair-DA condition in Fig. 9) was loaded further until 10^7 cycles and the sample did not fail. Thus, it is less likely that the choice of 5×10^6 as fatigue run-out will affect the present research finding.

A power-law model akin to the Basquin's equation [12] was adopted for fitting the data (only applicable to the failed samples).

$$\sigma_{max} = aN_f^b$$

where a and b are fitting constants, and the dashed lines correspond to the power-law fit representing the fatigue performance of the investigated materials, with the derived parameters as well as the R-squared values summarised in Table 2.

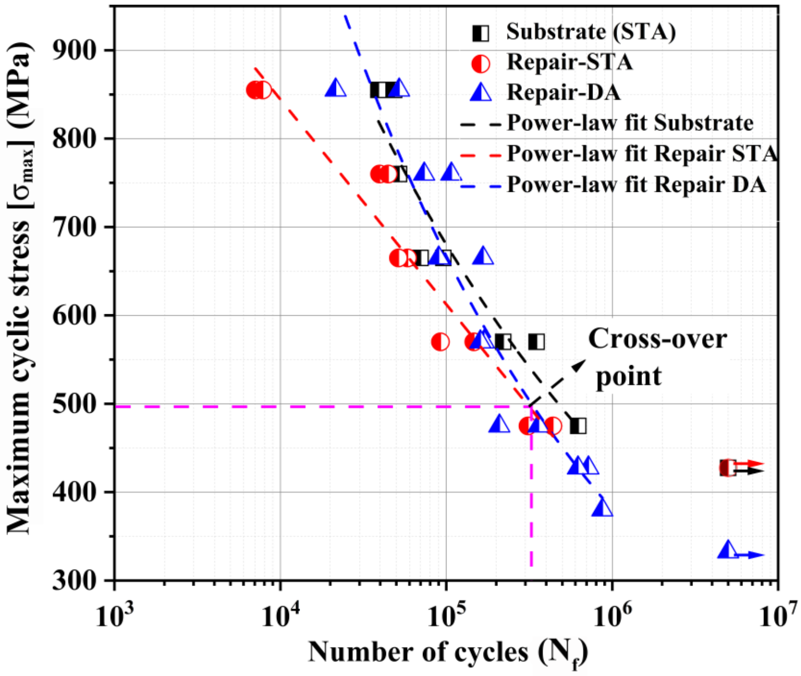

Fig 9: Power-law fit S-N curves, and fatigue data points of the DED repaired IN718 joint in both the STA and DA conditions in comparison with the wrought IN718 in STA condition. The cross-over point of the STA and DA curves is at the fatigue stress level of $\boldsymbol{\sigma_{max}}$=500 MPa.

Table 2: Parameters derived from the HCF fatigue testing

Material condition	**a**	**b**	**Adjusted R-squared**
IN718 – DA	8415.53	-0.22	0.88
IN718 – STA	2965.87	-0.14	0.89
Wrought – STA	6641.70	-0.20	0.89

The general trend is that N_f increased with the decreasing cyclic stress level of σ_{max}. The wrought substrate generally outperformed the DED IN718 repaired joint in both the STA and DA conditions. In terms of the fatigue limit, the DED IN718 repaired joint in the STA condition had a similar value of $\sigma_{\max}$=430 MPa when compared to the wrought IN718 in the STA condition, whereas the IN718 in the DA condition was about 100 MPa lower. Such a significant difference in the fatigue limit between the STA and DA conditions for the DED IN718 repaired joint was not expected as the monotonic tensile strength and the microhardness of the DED samples was very similar (Table 1 and Fig 7a). Moreover, at low fatigue stress levels, the STA condition of the DED IN718 repaired joint seemed to show a better fatigue behaviour than the DA condition. At high-stress levels (60 pct to 90 pct of the yield strength), however, the DA samples performed better than the STA, and to some extent, the fatigue property became comparable to the wrought IN718. The fatigue *S-N* plot shows a cross-over point at the fatigue stress level of $\sigma_{\max}$=500 MPa, where the relative fatigue performance of the two heat treatment conditions (STA vs. DA of the DED repaired joint) switched over.

3.4. Interrupted fatigue tests

Interrupted fatigue tests were performed using two different maximum cyclic stress levels; one above ($\sigma_{\max}$ = 665 MPa, ~70 % of average yield strength, abbreviated as YS) and the other below ($\sigma_{\max}$ = 428 MPa, ~45% of YS) the cross-over point as shown in Fig 9. Both the STA and DA conditions were considered, and hence in total, four interrupted fatigue tests were conducted. These tests were interrupted at various percentage of the average life (N_f) ranging from 10% to 90%, to capture the crack initiation and propagation behaviour with the aid of SEM examination. Overall, these interrupted tests revealed four main preferential sites for cracking, with representative SEM micrographs in Fig. 10a – Fig. 10f including: (i) grain boundaries of the substrate close to the substrate-to-deposit interface (Fig. 10a and Fig. 10b); (ii) carbides in the heat-affected zone of the substrate or DED deposit zone (Fig. 10d); (iii) transgranular type (Fig. 10c); and (iv) Laves and δ phases in the DED deposit zone (Fig. 10e and Fig. 10f). In addition, no fatigue crack was associated with the pores. Such an observation is consistent with the HCF work on SLM [42] and DED [19] IN718. Especially, after reducing the porosity level from 0.39% to 0.08% and the size to somewhere between 40 μm and 100 μm by hot isostatic pressing, no improvement in fatigue performance of SLM IN718 was observed [42].

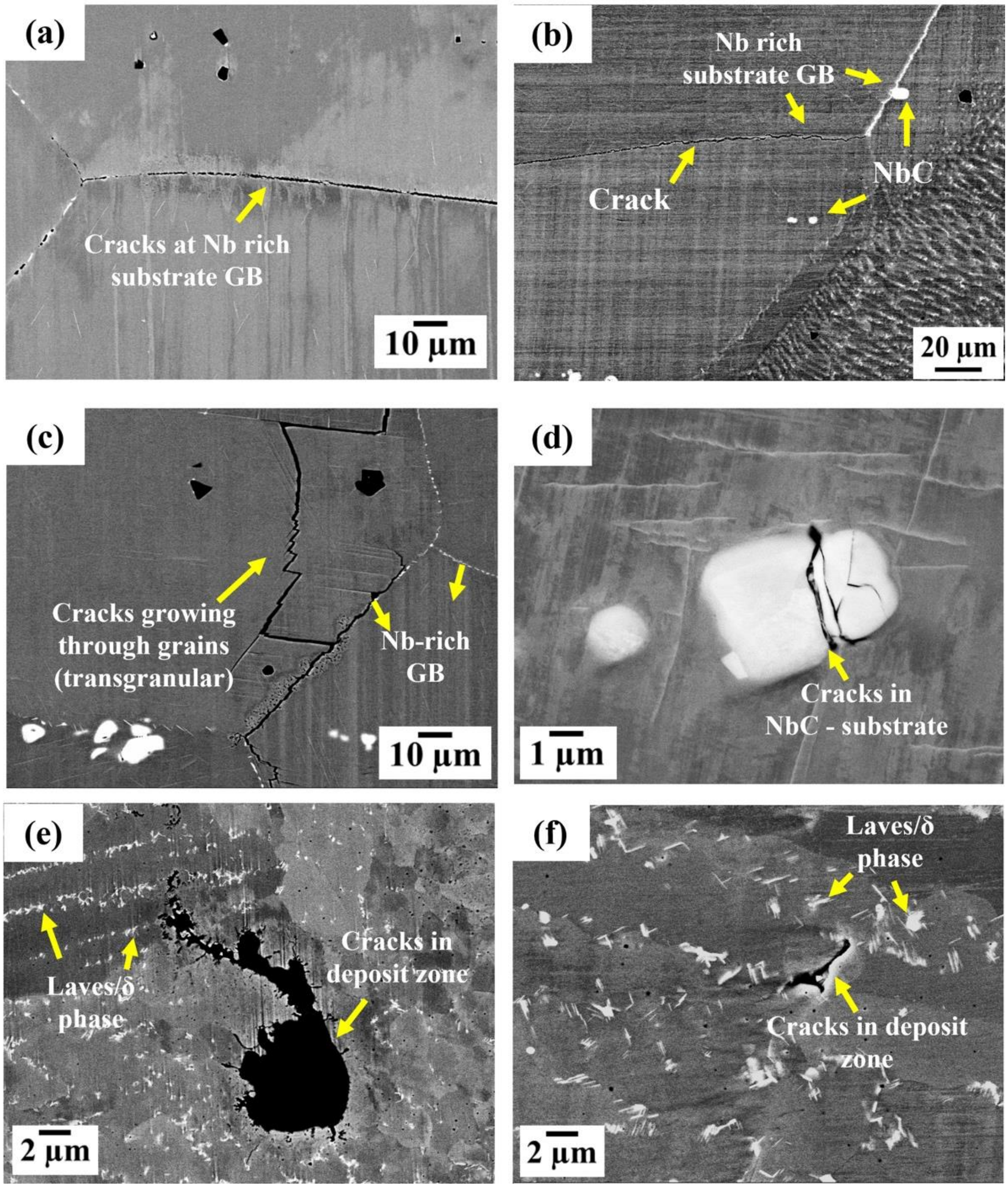

Fig 10: Fatigue microcracks initiating at various preferential sources on the sample surface, including (a) and (b) grain boundary of the substrate wrought near the substrate-to-deposit interface; (c) transgranular cracks and (d) broken carbides as observed in the substrate; (e) and (f) broken Laves and δ phases in the deposit zone.

Fig 11(a – d) show the development of a crack with the increasing number of cycles for the DA specimen tested at σ_{max} = 665 MPa. The corresponding Fig 11e and Fig 11f show the quantitatively measured size of fatigue cracks and their number density in relation to the characteristic cracking sites. In detail, a fatigue crack was observed at the interrupting cycle of 40% N_f, Fig 11a, and such a crack developed from a grain boundary in the substrate near the deposit-to-substrate interface. With the increased fatigue cycles (60% N_f), the fatigue crack followed an intergranular propagation path, extending to the nearby grains, Fig 11b.

Transgranular crack growth started to appear with the further increased cycles, and many micro-cracks were formed ahead of the major dominant crack, followed by their coalescence into a fatal crack, and finally resulted in the fatigue fracture through the substrate, Fig 11c and 11d. The total crack length and the number density of cracks increased continuously to ~325 μm/mm^2 (Fig 11e) and ~6 cracks/mm^2 (Fig 11f), respectively, until reaching a plateau at 60% N_f. In the initial stage of up to 40% N_f, the high crack density and fast growth rate were observed in the substrate. In addition, broken metal carbides were seen in the deposit zone, however, the associated cracks did not grow. To summarise, the fatal fatigue crack occurred from the grain boundary of the substrate close to the substrate-to-deposit interface for the DA condition under the high-stress fatigue loading of σ_{max}=665 MPa and R=0.1.

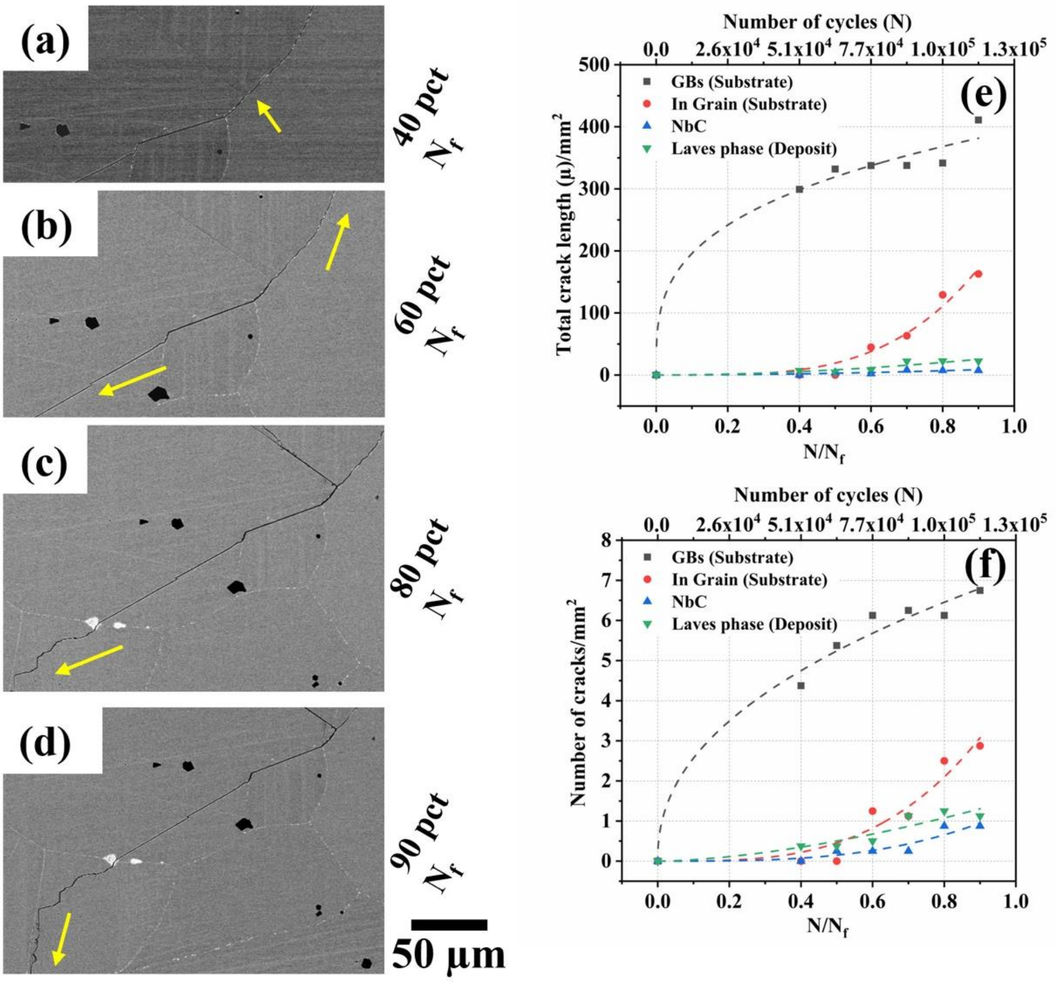

Fig 11: Representative SEM micrographs showing the development of a crack in DA specimen tested at $\boldsymbol{\sigma}_{\mathbf{max}}$ = 665 MPa in various stages of fatigue life: (a) 40% $\boldsymbol{N_f}$; (b) 60% $\boldsymbol{N_f}$; (c) 90% $\boldsymbol{N_f}$; (d) 90% $\boldsymbol{N_f}$; quantitative measurements of (e) total crack length and (f) number density of fatigue cracks growing from different sources on the specimen surface.

Fig 12a – Fig 12c show the crack development in the STA specimen tested at the same fatigue stress level (665 MPa) as the DA specimen (Fig 11). Despite some DED process induced defects appeared in the deposit region, they did not contribute to the fatal fatigue crack initiation at the later stage. In this case, the major transgranular crack was developed after 60% N_f in the deposit region, most likely a surface crack initiation as revealed in two-dimensional view, Fig 12c. The distance of the observed defect to the specimen surface in Fig 12c was about four to five times greater than the size of the defect, belonging to the internal defect type [38] and thereby having a limited effect on surface fatigue cracking. A high magnification micrograph showing cracks at broken δ and Laves phases is shown in Fig 12d.

Based on the quantitative assessment of cracking behaviour, it was found that cracks appeared simultaneously in the substrate grain boundaries and the deposit zone through the Laves and δ phases, Fig 12e and Fig 12f. Till 40% N_f, the crack growth predominantly occurred through the substrate grain boundary with the total crack length measured ~80 μm/mm^2, significantly higher than that observed in the deposit zone (~20 μm/mm^2). However, after 40% N_f, the Laves and δ phases along the dendritic arm in the deposit zone provided an easy crack path, causing a higher total crack length in Fig 12e. This resulted in the fatal crack development with a very fast rate in the deposit zone, Fig 12c, leading to the failure of the DED IN718 joint. In this case, the specimen failed prematurely, with the fatigue life being only 65% of the anticipated N_f. A repeat test was conducted, and the specimen failed at a similar fatigue life, about 50,000 cycles (~70% of the anticipated N_f). This observation suggests that the crack initiation and propagation of the STA specimen are very sensitive to the microstructure of the DED deposit region. To summarise, the fatal fatigue crack occurred at the DED deposit region, where the characteristic distribution of Laves and δ phases contributed to the crack path tortuosity for the STA condition under the high-stress fatigue loading of $\sigma_{\max}$= 665 MPa and R=0.1.

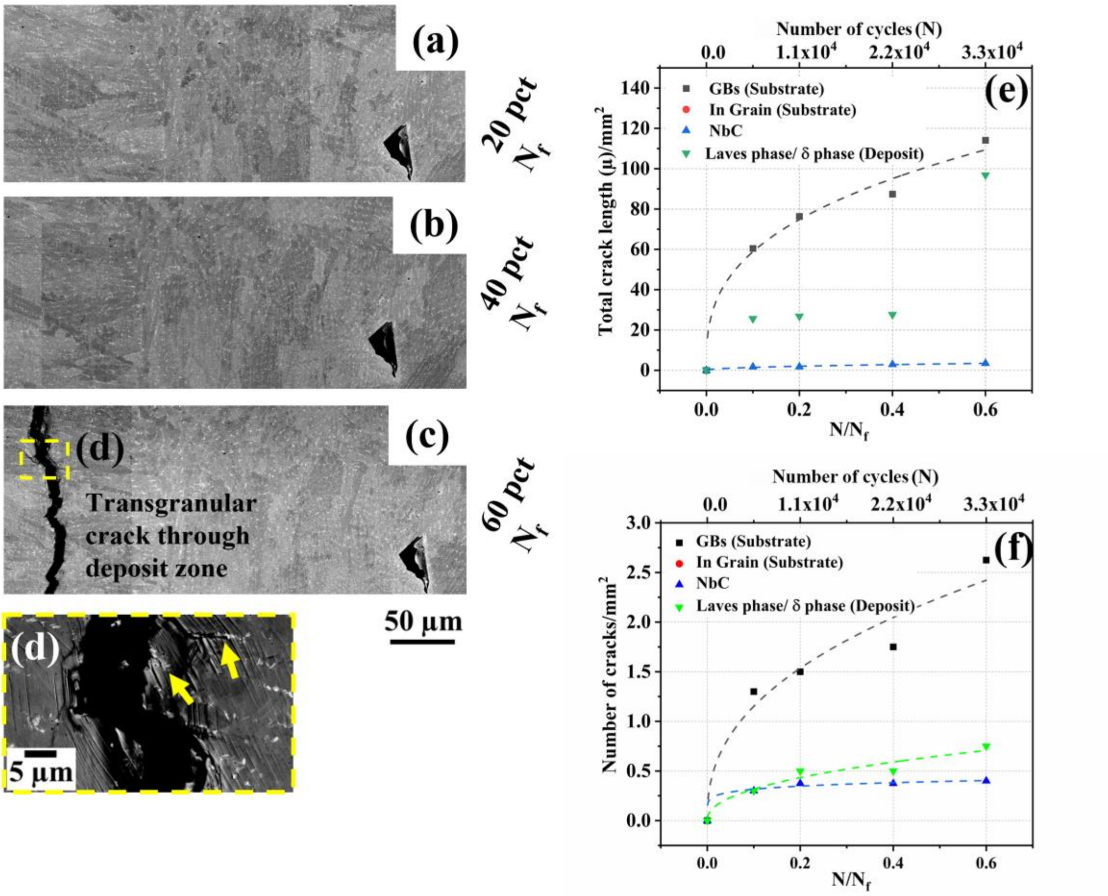

Fig 12: Representative SEM micrographs illustrating the development of a crack in STA specimen near the final fracture region, specimen tested at $\boldsymbol{\sigma}_{\mathbf{max}}$ = 665 MPa, in various stages of fatigue life: (a) 20% $\boldsymbol{N_f}$; (b) 40% $\boldsymbol{N_f}$; (c) 60% $\boldsymbol{N_f}$; (d) a high magnification micrograph of the deposit zone, with the arrows indicating broken Laves phases and δ phases in the vicinity of the fatigue crack; quantitative measurements of (e) total crack length and (f) number density of fatigue cracks. For the characteristic crack at deposit zone associated with Laves and δ phases, no measurable change in crack length was found between 10% to 40% $\boldsymbol{N_f}$. Thus, the curve fitting is not given in (e) to avoid misunderstanding.

For the interrupted fatigue specimen in the DA condition, tested at $\sigma_{\max}$ = 428 MPa (low fatigue stress level), the early crack initiation occurred at the grain boundaries of the substrate, Fig 13a, at 10% N_f. A transgranular crack appeared in the substrate after 40% N_f, Fig 13b. At 70% and 90% N_f, the crack propagated into the deposit zone from the substrate, Fig 13c and Fig 13d, respectively. Both the increase in the total crack length and the number density of cracks can be seen in Fig 13e and Fig 13f, respectively, with a far more frequent observation of cracks initiated from the grain boundaries at the substrate wrought IN718. The crack propagation followed a transgranular path, acting as the major crack. As a result, the number density of transgranular cracks did not increase, as shown in Fig 13f. The cracks grew into the deposit zone only after significant growth through the substrate at 60% – 70% N_f. For the STA condition, the specimen tested at the same stress level did not fail at this stress level (i.e. fatigue run-out). Representative SEM micrographs of fatigue cracks are shown in Fig 14a and Fig 14b. A crack first appeared at the grain boundary of the substrate (20% N_f, Fig 14a); however, the crack did not grow even after the 70% N_f, Fig 14b.

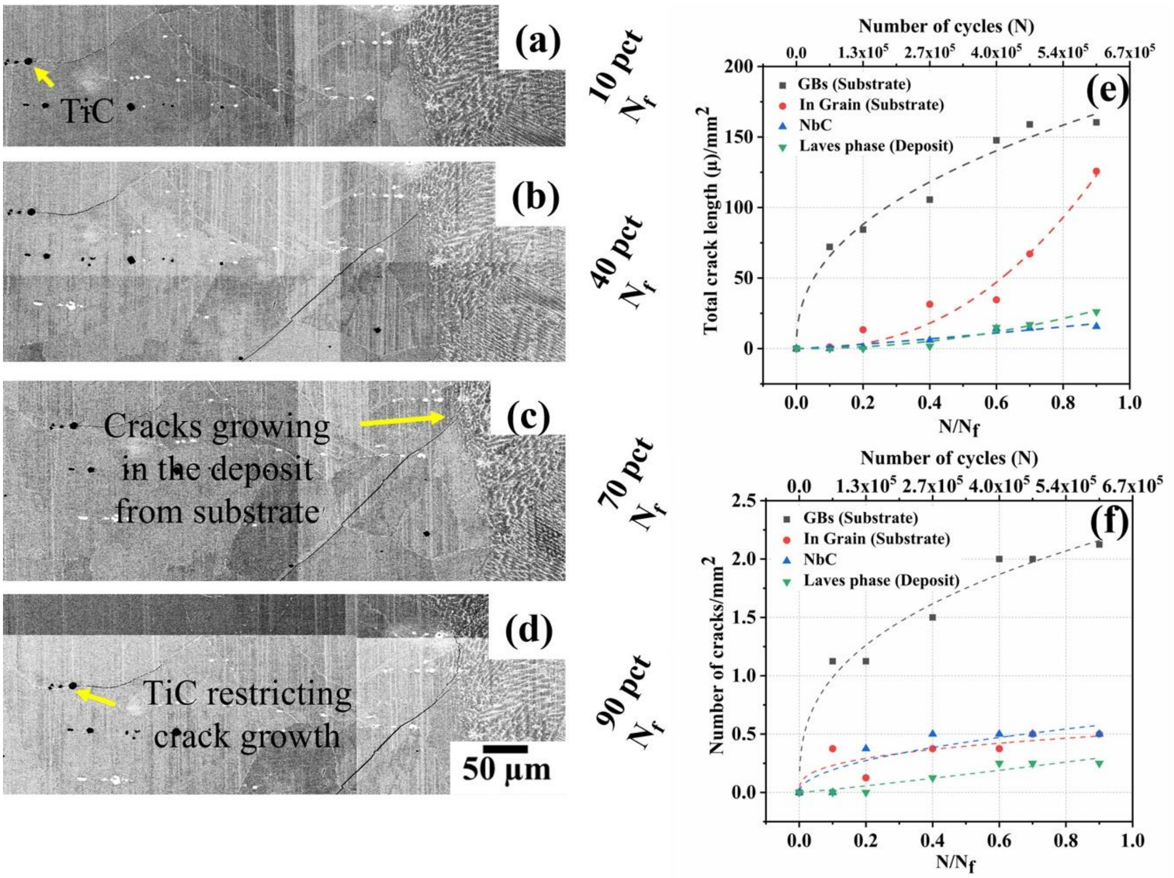

Fig 13: Representative SEM micrographs illustrating the development of crack in DA specimen tested at $\boldsymbol{\sigma}_{\mathbf{max}}$ = 428 MPa in various stages of fatigue life: (a) 10% $\boldsymbol{N_f}$; (b) 40% $\boldsymbol{N_f}$; (c) 70% $\boldsymbol{N_f}$; (d) 90% $\boldsymbol{N_f}$; quantitative measurements of (e) total crack length and (f) number density of fatigue cracks.

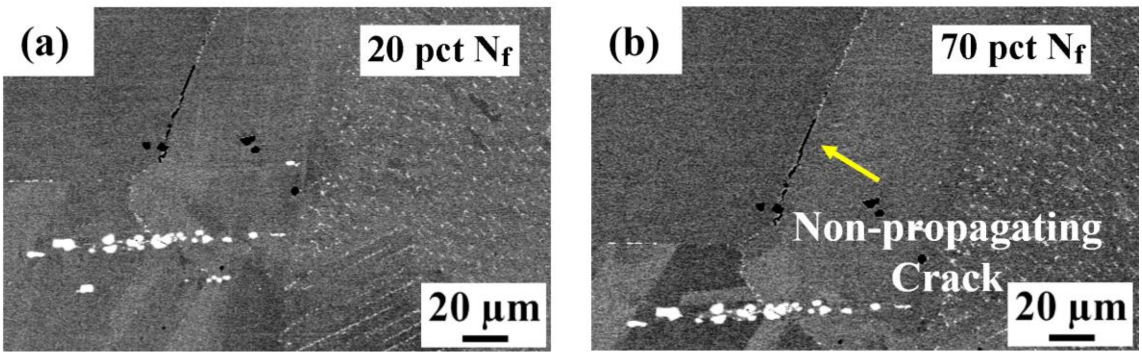

Fig 14: Representative SEM micrographs showing a non-propagating fatigue crack in STA specimen tested at $\boldsymbol{\sigma}_{\mathbf{max}}$ = 428 MPa interrupted at: (a) 20% $\boldsymbol{N_f}$; (b) 70% $\boldsymbol{N_f}$.

In the present work, the coarse NbC (e.g. Fig. 10d) has been identified as the preferential fatigue crack initiation site; this applies to both the STA and DA conditions of the DED repaired joint. However, the quantitative measurements made on the interrupted fatigue test specimens helped to elucidate that such a crack did not propagate to the required length to trigger the final fatigue failure, despite its early crack initiation. Inclusions such as carbides are recognised as the important factor affecting the fatigue performance in IN718, however, such a detrimental role is pronounced at cryogenic temperatures [46] and at high stress levels (i.e. low-cycle fatigue, with the stress level of above YS) [47,48].

3.5. Fatigue failure mechanisms

To corroborate the fatigue failure mechanism as observed in the interrupted specimens for the high and low fatigue stress levels and STA and DA heat treatment conditions, the SEM cross-sectional view of the fractured surface, as well as SEM fractography, were conducted. Specimen tested under the σ_{max} = 665 MPa represents the high-stress condition, while that tested at σ_{max} = 475 MPa represents the low-stress condition. The latter was chosen as the specimen tested at σ_{max} = 428 MPa in the STA condition exhibited fatigue run-out (Fig 9). For both the high and low cyclic stresses, the DA specimens exhibited cracks propagating through the grain boundaries and twin boundaries at the substrate, as shown in Fig 15a and Fig 15d, respectively. Some secondary grain boundary cracks near the repaired joint were observed, Fig 15d. On the contrary, the STA specimens showed the final failure occurring in the DED deposit zone near the repaired joint, Fig 15b for the high-stress condition, while Fig 15e for the low-stress test condition, and fractured Laves and δ phases can be seen at the vicinity of the fracture surface (Fig 15c, Fig 15f). It is likely that with increasing fatigue cycles, the fractured Laves and δ phases, along with the deformation of the γ-matrix, led to the formation of microvoids, which provided an easy crack path, ultimately triggering the failure of the joint.

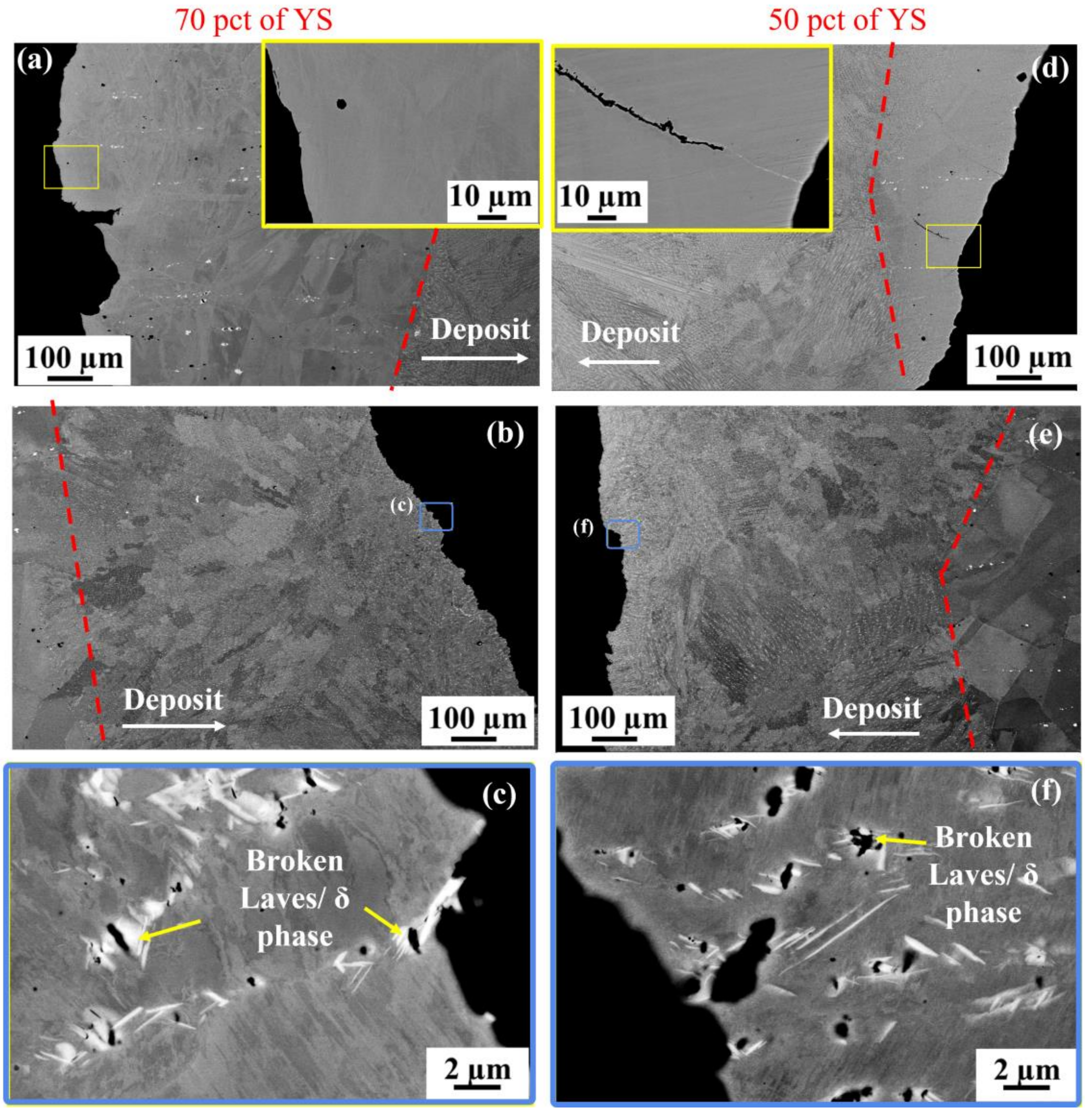

Fig 15: Cross-sectional view of the region near to the final fracture of the specimen tested at the maximum cyclic stress of (a) 665 MPa in DA condition, with failure occurring in the substrate; (b) 665 MPa in STA condition with failure occurring in the deposit zone; (d) 475 MPa in DA condition, with failure occurring in the substrate; (e) 475 MPa in STA condition, with failure occurring in the deposit zone; (c) and (f) high magnification micrograph of (b) and (e), respectively, showing the presence of broken δ and Laves phases near the fracture surface.

Fig 16 summarises the SEM fractography of fatigue failed specimens. The failure occurred in the substrate of the DED repaired joint in the DA condition while in the deposit zone in the STA condition. Therefore, the fracture surfaces are representative of the features of the wrought IN718 in the top two rows, Fig 16a to Fig 16f, whilst the DED deposit zone in the bottom two rows, Fig 16g to Fig 16l. Overall, the fracture surfaces exhibited characteristic features of facets, secondary cracks, striation marks, deposition defects, and dimples typical of microvoid coalescence. The dimples of the STA specimen that failed in the deposit zone were finer, and the overall fracture surface was smoother when compared to those of the DA specimen that failed in the substrate region.

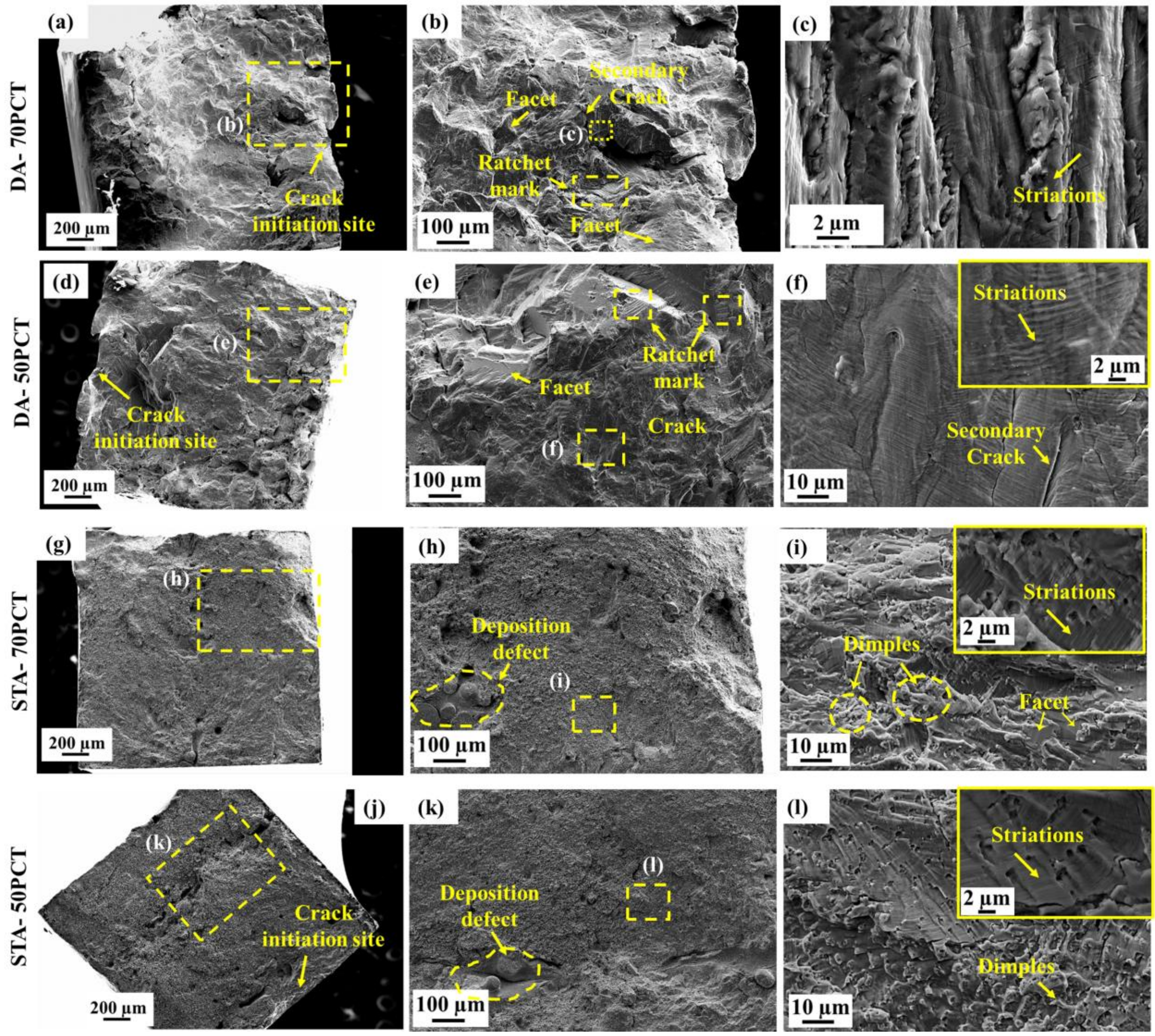

Fig 16: SEM fractography showing fatigue crack initiation sites, facets, microcracks on the fractured surface, and fatigue striations: (a), (b) and (c) DA specimen tested at $\boldsymbol{\sigma}_{\mathbf{max}}$ = 665 MPa; (d), (e) and (f) DA specimen tested at $\boldsymbol{\sigma}_{\mathbf{max}}$ = 475 MPa; (g), (h) and (i) STA specimen tested at $\boldsymbol{\sigma}_{\mathbf{max}}$ = 665 MPa; (j), (k) and (l) STA specimen tested at $\boldsymbol{\sigma}_{\mathbf{max}}$ = 475 MPa.

In the DA condition of Fig 16b and Fig 16e, crystallographic facets were observed after the surface crack initiation. Such facets have been reported in the room-temperature HCF study of the wrought IN718 and AM IN718 [28,49–52]. Ratchet marks were observed on the fracture surface, and their presence can be attributed to the multiple cracks propagating on parallel planes interconnected via secondary perpendicular cracks [51]. In addition to the dimples, fatigue striations appeared on the fracture surface. The specimen in STA condition exhibited presence of deposition defects such as porosities, lack of fusion located on the fracture surface, Fig 16h and Fig 16k. The surface exhibited a combination of ductile and brittle micro-mechanisms, i.e., facets and dimples (intergranular and transgranular), Fig 16i, highlighting the complex nature of the DED IN718 microstructure.

4. Discussion

4.1. Rationalisation of the fatigue performance with microstructure observation

For a polycrystalline material, it is recognised that, below the fatigue limit, the accumulation of fatigue damage during cyclic loading is dynamically balanced by the progressive strengthening due to strain ageing [12], and the fatigue failure occurs when the damage predominates over strengthening. Grain boundaries of the substrate wrought IN718 are the favourable site for crack initiation and play a major role in the fatigue damage initiation, regardless of the heat treatment conditions. However, the cyclic failure mechanism differs when the maximum cyclic stress is above or below the cross-over point of Fig 9. One of the features identified in the present study, which is believed to weaken the grain boundary strength under HCF loading, is the Nb-rich liquid films at the grain boundaries of the substrate near the deposit-to-substrate interface. Due to the high temperatures experienced during welding or AM processes, the secondary phases, such as intermetallic phases and carbides, suffer local melting at elevated temperatures. Moreover, due to the rapid heating and cooling rates, the second-phase particles may not be completely dissolved when the eutectic temperature is reached in the heat-affected zone. The metastable liquid may thus nucleate heterogeneously at the interfaces between the remaining second-phase particles and the matrix, followed by rapid melting of the second-phase particles and part of the surrounding matrix [53]. In the case of IN718, NbC carbides liquate over a range of temperatures, initiating at a temperature range of 1200ºC to 1215ºC, below the γ-carbide eutectic L → (γ + NbC) temperature of 1250ºC [54]. Thus, liquid on the grain boundaries in the heat-affected zone originates due to constitutional liquation of the NbC [55], and the quenched-in liquid formed solidifies to a composition similar to Laves phase. These are identified as the Nb-rich substrate grain boundaries as shown in Fig 5d and Fig 6d. The inability of these liquid films to accommodate the stresses results in crack formation at the substrate grain boundaries near the deposit-to-substrate interface as shown in Fig 10a and Fig 10b.

For the interrupted test performed on the STA condition with the σ_{max} = 428 MPa, which is just below the fatigue limit, non-propagating microcracks at the grain boundary of the substrate region are observed in Fig 14a and Fig 14b. By comparison, for the DA condition tested at a similar stress level, the microcracks initiated at the grain boundary of the substrate region can propagate, Fig 13(a – c). Therefore, the threshold stress above which those already initiated microcracks can propagate determines the fatigue limit. This seems to agree with the higher fatigue limit in the STA condition when compared to DA.

At the high cyclic stress region of Fig 9, the wrought material as well as the DED repaired joint in the DA condition exhibit higher fatigue life than the DED repaired joint in the STA condition. The deposit zone has a significantly smaller grain size of heterogeneous distribution and no annealing twins compared to the wrought material that has coarse equiaxed grains. Since the crystallographic texture is weak for both the deposit zone and substrate (Fig 3), various microstructural features in the deposit zone, substrate, and the deposit-to-substrate interface likely act as competing factors influencing fatigue performance. As shown in Fig 5c, in the DA condition, the substrate grain boundaries in the heat-affected zone (i.e. close to the deposit region but still in the wrought material) are devoid of any δ phase, but with the Laves phase presented at the substrate grain boundaries and in the inter-dendritic region in the deposit zone. The work on IN718 showed that the Laves phase has poor plastic deformation capability during tensile loading [5,56]. The γ matrix possesses higher deformability and often leads to the formation of stress concentration sites at the interface between the γ matrix and Laves phase. As the cracks initiate and grow through the substrate grain boundaries at higher loads, the failure mechanism in the DA specimen mimicked the failure mechanism of wrought IN718.

From uniaxial tensile tests reported in Fig 8, the STA condition exhibits improved ductility compared to the DA specimen. While it has been observed that the δ phase improves fatigue properties in Ni-base superalloys by arresting crack propagation [14,29], this only occurs at low-stress levels. An et al. [13] reported that the δ phase degraded the fatigue life in the wrought IN718, and such phenomenon was attributed to the morphology of the δ phase. The Laves phase and δ precipitates are both enriched in Nb, while the surrounding matrix is depleted of Nb, resulting in a lack of γ'' strengthening phase [30,57]. Therefore, near the δ phase, a region depleted in γ'' is formed that may act as the micro-void initiation site. Moreover, a higher volume fraction of the δ phase in the microstructure would consume the Nb for γ'' formation during the subsequent ageing treatment. During cyclic loading, dislocations are easily piled up around the long needle-like δ phase, which leads to high-stress concentration, and subsequent δ phase debonding from the matrix and helps easy crack propagation along the long needle-like δ phase surrounded by the precipitate-free-zone. Therefore, the heterogeneous distribution of the needle-like δ phase and higher volume fraction in the deposit zone likely made it easier to induce stress concentration sites at high-stress levels, and hence the STA specimen at high fatigue stress failed in the deposit zone. At low-stress levels, the debonding of the δ/Laves phase from the γ matrix did not happen.

4.2. Fatigue data comparison

The fatigue limit of wrought IN718, as reported in the Aerospace Structural Metals Handbook (AD737973) [58], is ~500 MPa, which is 75 MPa higher than the wrought IN718 considered in the present study. Such difference in the fatigue strength can be attributed to grain size difference with the former of ~35 µm while the latter of ~90 µm. HCF tests on wrought IN718 with different grain sizes by Ono et al. [59] and Kevinsanny et al. [60] revealed higher fatigue life corresponded to the higher strength and hardness in the fine-grained samples compared to the coarse-grained samples. It is well known that grain boundaries hinder the slip transfer between grains, leading to the formation of pile-ups and hardening as the grain size decreases [12]. Therefore a fine-grained material with higher hardness and strength would provide higher resistance to plastic deformation, and hence improved fatigue strength is observed [61].

The fatigue test results from the current study are compared to the literature data. For a valid comparison, only the room temperature HCF test data obtained at R = 0.1 and using hourglass specimen geometry are included. Fig 17a compares the present results with the fatigue data of IN718 manufactured by various AM technologies with a fatigue loading axis parallel to the build direction [19,52]. The fatigue limit estimated by Witkin et al. [52] on SLM IN718 was ~ 450 MPa (see Table 2 [52]), tested at R = 0.1, which matches well with the observed results in the present investigation on the STA specimens while being ~100 MPa higher than the DA condition. A slightly higher fatigue limit of ~480 MPa compared to the results of the present STA specimens was reported by Amsterdam et al. [19] for the DED fabricated IN718 specimens that were solution annealed at 1093ºC and then aged. A solution treatment temperature of ~1100ºC dissolved the Laves and δ phases in SLM IN718 [62], which could be the reason for the improved fatigue performance in the work by Amsterdam et al. [19]. The fatigue life observed by Balachandramurthi et al. [63] in electron beam melted (EBM) IN718 was consistently inferior compared to both the DA and STA specimens in the present work, tested at similar maximum stress levels.

Fig 17b shows the data comparison with the welding repaired IN718 with the fatigue loading axis perpendicular to the weld centreline [30,31]. The DED-repaired IN718 joint tested at both the DA and STA conditions performed better than the TIG welded IN718 reported by

Alexopoulos et al. [31]. Compared to the results observed in the current investigation, Sivaprasad et al. [30] reported superior fatigue properties of the TIG welded IN718 tested in DA and STA conditions. The difference in the fatigue properties compared to the present study can be attributed to the innate material properties of the IN718 substrate as depicted by significantly higher fatigue limit (~750 MPa) of the substrate (wrought) IN718 under investigation (Fig 17b). However, the fatigue performance of TIG welded specimens reported by Sivaprasad et al. [30] tested in DA and STA conditions showed a similar trend as reported in the present study. At higher maximum stress levels, the DA fatigue performance is better, whereas, at low-stress levels, better fatigue performance and higher fatigue limit are observed for the STA specimens.

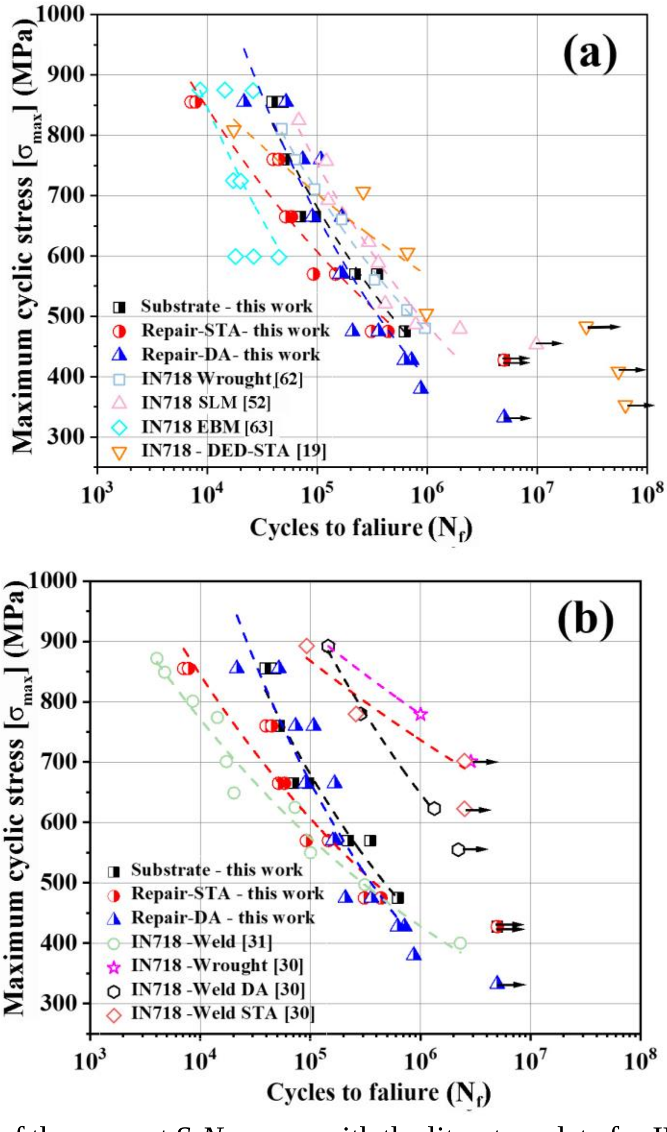

Fig 17: Comparison of the present *S*-*N* curves with the literature data for IN718: (a) comparison with AM IN718 components; and (b) comparison with welding repaired IN718. For comparison purposes, all the fatigue data were generated at R = 0.1 and room temperature.

It can be summarised from the present investigation and other reports available in the literature that wrought IN718 generally outperforms IN718 processed via various AM techniques or fusion welding. The primary reason for the difference in fatigue performance can be related to the difference in the microstructure due to various processing methods. Laser-based AM techniques can be broadly classified as DED or SLM processes. High cooling rates of $10^3 – 10^5$ K/s are achieved during DED and $10^5 – 10^7$ K/s in SLM processing [64]. Similarly, high cooling rates $>10^2$ K/s are achieved during welding processes [23]. The non-equilibrium phases formed during AM processes and welding results in the deterioration of fatigue properties. Post-processing heat treatments are often employed to improve fatigue properties. In repair processes (welding/AM), to prevent grain coarsening in the base metal, the solution treatment temperatures are generally restricted to 980ºC. The solution treatment at 980ºC results in the formation of δ precipitates along with the retained Laves phase. The formation of δ precipitates results in slight softening of the material, thereby deteriorating high-stress HCF properties, however, at stresses below 50% of yield strength, δ precipitates are found to be beneficial for fatigue properties.

5. Conclusion

IN718 repaired joint, processed via direct energy deposition (DED), in both the solution treated and aged (STA) and directly aged (DA) conditions, has been assessed with the fatigue loading axis being perpendicular to the interface between the wrought substrate and the DED deposit. The major conclusions are:

1. Performing the post-processing heat treatment is essential for IN718 repairs using DED processing to eliminate the low-strength heat-affected zone, which can extend up to 800 μm in the substrate near the deposit-to-substrate interface.
2. The wrought substrate generally outperforms the DED repaired joint under HCF testing. However, the performance of the repaired joint is comparable to AM IN718 as reported in the literature and, in some cases, better than the welding repaired IN718.
3. At high fatigue stress levels, the DA samples outperform the STA samples, whereas, at low-stress levels, the STA samples perform better. Therefore, a cross-over point appears in the *S-N* curves when comparing the DA with STA conditions. The fatigue failure occurs in the substrate for the DA condition, whereas in the deposit zone for the STA condition.

4. The Nb-rich film developed along the grain boundaries of the substrate wrought IN718 near the substrate-to-deposit interface, acts as the crack initiation site. In the STA condition, the needle-shaped δ precipitates coupled with the Laves phase are effective in arresting cracks at the low fatigue stress level, however, at high-stress levels, they provide preferential sites to trigger the microcrack initiation and propagation.

Acknowledgement

Riddhi Sarkar acknowledges Dr. David Parfitt, Coventry University and the Deakin University Advanced Characterisation Facility for technical support. Bo Chen acknowledges financial supports by the UK's Engineering and Physical Sciences Research Council, EPSRC First Grant Scheme EP/P025978/1 and Early Career Fellowship Scheme EP/R043973/1.

References

[1] C. Guévenoux, S. Hallais, Y. Balit, A. Charles, E. Charkaluk, A. Constantinescu, Plastic strain localization induced by microstructural gradient in laser cladding repaired structures, Theor. Appl. Fract. Mech. 107 (2020) 102520. https://doi.org/10.1016/j.tafmec.2020.102520.

[2] S. Sui, J. Chen, R. Zhang, X. Ming, F. Liu, X. Lin, The tensile deformation behavior of laser repaired Inconel 718 with a non-uniform microstructure, Mater. Sci. Eng. A. 688 (2017) 480–487. https://doi.org/10.1016/j.msea.2017.01.110.

[3] S. Sui, J. Chen, X. Ming, S. Zhang, X. Lin, W. Huang, The failure mechanism of 50% laser additive manufactured Inconel 718 and the deformation behavior of Laves phases during a tensile process, Int. J. Adv. Manuf. Technol. 91 (2017) 2733–2740. https://doi.org/10.1007/s00170-016-9901-9.

[4] E. Hosseini, V.A. Popovich, A review of mechanical properties of additively manufactured Inconel 718, Addit. Manuf. 30 (2019) 100877. https://doi.org/10.1016/j.addma.2019.100877.

[5] E. Chlebus, K. Gruber, B. Kuźnicka, J. Kurzac, T. Kurzynowski, Effect of heat treatment on the microstructure and mechanical properties of Inconel 718 processed by selective laser melting, Mater. Sci. Eng. A. 639 (2015) 647–655. https://doi.org/10.1016/j.msea.2015.05.035.

[6] J.H. Yi, J.W. Kang, T.J. Wang, X. Wang, Y.Y. Hu, T. Feng, Y.L. Feng, P.Y. Wu, Effect of laser energy density on the microstructure, mechanical properties, and

deformation of Inconel 718 samples fabricated by selective laser melting, J. Alloys Compd. 786 (2019) 481–488. https://doi.org/10.1016/j.jallcom.2019.01.377.

[7] D. Zhang, W. Niu, X. Cao, Z. Liu, Effect of standard heat treatment on the microstructure and mechanical properties of selective laser melting manufactured Inconel 718 superalloy, Mater. Sci. Eng. A. 644 (2015) 32–40. https://doi.org/10.1016/j.msea.2015.06.021.

[8] D. Zhang, W. Niu, X. Cao, Z. Liu, Effect of standard heat treatment on the microstructure and mechanical properties of selective laser melting manufactured Inconel 718 superalloy, Mater. Sci. Eng. A. 644 (2015) 32–40. https://doi.org/10.1016/j.msea.2015.06.021.

[9] W. Huang, J. Yang, H. Yang, G. Jing, Z. Wang, X. Zeng, Heat treatment of Inconel 718 produced by selective laser melting: Microstructure and mechanical properties, Mater. Sci. Eng. A. 750 (2019) 98–107. https://doi.org/10.1016/j.msea.2019.02.046.

[10] H. Qi, M. Azer, A. Ritter, Studies of standard heat treatment effects on microstructure and mechanical properties of laser net shape manufactured INCONEL 718, Metall. Mater. Trans. A Phys. Metall. Mater. Sci. 40 (2009) 2410–2422. https://doi.org/10.1007/s11661-009-9949-3.

[11] S. Sui, J. Chen, E. Fan, H. Yang, X. Lin, W. Huang, The influence of Laves phases on the high-cycle fatigue behavior of laser additive manufactured Inconel 718, Mater. Sci. Eng. A. 695 (2017) 6–13. https://doi.org/10.1016/j.msea.2017.03.098.

[12] G.E. Dieter, Mechanical metallurgy., McGraw-Hill, New York, 2011. https://doi.org/10.5962/bhl.title.35895.

[13] J. An, L. Wang, Y. Liu, W. Cai, X. Song, The role of δ phase for fatigue crack propagation behavior in a Ni base superalloy at room temperature, Mater. Sci. Eng. A. 684 (2017) 312–317. https://doi.org/10.1016/j.msea.2016.12.029.

[14] S. Li, J. Yang, J. Zhuang, Q. Deng, J. Du, X. Xie, B. Li, Z. Xu, Z. Cao, Z. Su, C. Jiang, The Effect of Delta-Phase on Crack Propagation Under Creep and Fatigue Conditions in Alloy 718, in: Superalloys 718, 625, 706 Var. Deriv., TMS, 1994: pp. 545–555. https://doi.org/10.7449/1994/Superalloys_1994_545_555.

[15] S. Gribbin, S. Ghorbanpour, N.C. Ferreri, J. Bicknell, I. Tsukrov, M. Knezevic, Role of grain structure, grain boundaries, crystallographic texture, precipitates, and porosity on fatigue behavior of Inconel 718 at room and elevated temperatures, Mater. Charact. 149 (2019) 184–197. https://doi.org/10.1016/j.matchar.2019.01.028.

[16] A.J. Sterling, B. Torries, N. Shamsaei, S.M. Thompson, D.W. Seely, Fatigue behavior

and failure mechanisms of direct laser deposited Ti-6Al-4V, Mater. Sci. Eng. A. (2016). https://doi.org/10.1016/j.msea.2015.12.026.

[17] N. Shamsaei, A. Yadollahi, L. Bian, S.M. Thompson, An overview of Direct Laser Deposition for additive manufacturing; Part II: Mechanical behavior, process parameter optimization and control, Addit. Manuf. 8 (2015) 12–35. https://doi.org/https://doi.org/10.1016/j.addma.2015.07.002.

[18] A. Yadollahi, N. Shamsaei, Additive manufacturing of fatigue resistant materials: Challenges and opportunities, Int. J. Fatigue. 98 (2017) 14–31. https://doi.org/10.1016/j.ijfatigue.2017.01.001.

[19] E. Amsterdam, Evaluation of the microstructure and mechanical properties of laser additive manufactured gas turbine alloys Ti-6Al-4V and, RTO AVT-163 Spec. Meet. (2009) 1–25.

[20] A. Yadollahi, N. Shamsaei, S.M. Thompson, A. Elwany, L. Bian, Effects of building orientation and heat treatment on fatigue behavior of selective laser melted 17-4 PH stainless steel, Int. J. Fatigue. (2017). https://doi.org/10.1016/j.ijfatigue.2016.03.014.

[21] A.R. Balachandramurthi, J. Moverare, N. Dixit, D. Deng, R. Pederson, Microstructural influence on fatigue crack propagation during high cycle fatigue testing of additively manufactured Alloy 718, Mater. Charact. 149 (2019) 82–94. https://doi.org/10.1016/j.matchar.2019.01.018.

[22] Y. Chen, K. Zhang, J. Huang, S.R.E. Hosseini, Z. Li, Characterization of heat affected zone liquation cracking in laser additive manufacturing of Inconel 718, Mater. Des. 90 (2016) 586–594. https://doi.org/10.1016/j.matdes.2015.10.155.

[23] S.G.K. Manikandan, D. Sivakumar, K.P. Rao, M. Kamaraj, Effect of weld cooling rate on Laves phase formation in Inconel 718 fusion zone, J. Mater. Process. Technol. 214 (2014) 358–364. https://doi.org/10.1016/j.jmatprotec.2013.09.006.

[24] Y. Mei, Y. Liu, C. Liu, C. Li, L. Yu, Q. Guo, H. Li, Effect of base metal and welding speed on fusion zone microstructure and HAZ hot-cracking of electron-beam welded Inconel 718, Mater. Des. 89 (2016) 964–977. https://doi.org/10.1016/j.matdes.2015.10.082.

[25] K.C. Chen, T.C. Chen, R.K. Shiue, L.W. Tsay, Liquation cracking in the heat-affected zone of IN738 superalloy weld, Metals (Basel). 8 (2018) 12–14. https://doi.org/10.3390/met8060387.

[26] R.G. Thompson, Microfissuring of Alloy 718 in the Weld Heat-Affected Zone, Jom. 40 (1988) 44–48. https://doi.org/10.1007/BF03258151.

[27] C.A. Huang, T.H. Wang, C.H. Lee, W.C. Han, A study of the heat-affected zone (HAZ) of an Inconel 718 sheet welded with electron-beam welding (EBW), Mater. Sci. Eng. A. 398 (2005) 275–281. https://doi.org/10.1016/j.msea.2005.03.029.

[28] Y. Ono, T. Yuri, N. Nagashima, H. Sumiyoshi, T. Ogata, N. Nagao, High-cycle fatigue properties of Alloy718 base metal and electron beam welded joint, Phys. Procedia. 67 (2015) 1028–1035. https://doi.org/10.1016/j.phpro.2015.06.196.

[29] K. Sivaprasad, S. Ganesh Sundara Raman, Influence of weld cooling rate on microstructure and mechanical properties of alloy 718 weldments, Metall. Mater. Trans. A Phys. Metall. Mater. Sci. 39 (2008) 2115–2127. https://doi.org/10.1007/s11661-008-9553-y.

[30] K. Sivaprasad, S.G.S. Raman, Influence of magnetic arc oscillation and current pulsing on fatigue behavior of alloy 718 TIG weldments, Mater. Sci. Eng. A. 448 (2007) 120–127. https://doi.org/10.1016/j.msea.2006.10.048.

[31] N.D. Alexopoulos, N. Argyriou, V. Stergiou, S.K. Kourkoulis, Fatigue behavior of Inconel 718 TIG welds, J. Mater. Eng. Perform. 23 (2014) 2973–2983. https://doi.org/10.1007/s11665-014-1028-2.

[32] ASTM, Standard Practice for Conducting Force Controlled Constant Amplitude Axial Fatigue Tests of Metallic Materials, Test. 03 (2002) 4–8. https://doi.org/10.1520/E0466-15.2.

[33] L. Zhu, Z. Xu, Y. Gu, Effect of lasechairr power on the microstructure and mechanical properties of heat treated Inconel 718 superalloy by laser solid forming, J. Alloys Compd. 746 (2018) 159–167. https://doi.org/10.1016/j.jallcom.2018.02.268.

[34] ASTM E8, ASTM E8/E8M standard test methods for tension testing of metallic materials 1, Annu. B. ASTM Stand. 4. (2010) 1–27. https://doi.org/10.1520/E0008.

[35] Z. Zhao, F. Zhang, C. Dong, X. Yang, B. Chen, Initiation and Early-Stage Growth of Internal Fatigue Cracking Under Very-High-Cycle Fatigue Regime at High Temperature, Metall. Mater. Trans. A Phys. Metall. Mater. Sci. 51 (2020) 1575–1592. https://doi.org/10.1007/s11661-020-05633-3.

[36] S. Majumdar, D. Bhattacharjee, K.K. Ray, On the Micromechanism of Fatigue Damage in an Interstitial-Free Steel Sheet, Metall. Mater. Trans. A. 39 (2008) 1676–1690. https://doi.org/10.1007/s11661-008-9537-y.

[37] H. Peng, Y. Shi, S. Gong, H. Guo, B. Chen, Microstructure, mechanical properties and cracking behaviour in a γ'-precipitation strengthened nickel-base superalloy fabricated by electron beam melting, Mater. Des. 159 (2018) 155–169.

https://doi.org/10.1016/j.matdes.2018.08.054.

[38] Y. Zhai, D.A. Lados, E.J. Brown, G.N. Vigilante, Understanding the microstructure and mechanical properties of Ti-6Al-4V and Inconel 718 alloys manufactured by Laser Engineered Net Shaping, Addit. Manuf. 27 (2019) 334–344. https://doi.org/https://doi.org/10.1016/j.addma.2019.02.017.

[39] R.G. Ding, Z.W. Huang, H.Y. Li, I. Mitchell, G. Baxter, P. Bowen, Electron microscopy study of direct laser deposited IN718, Mater. Charact. 106 (2015) 324–337. https://doi.org/10.1016/j.matchar.2015.06.017.

[40] R. Vincent, Precipitation around welds in the nickel-base superalloy, Inconel 718, Acta Metall. 33 (1985) 1205–1216. https://doi.org/10.1016/0001-6160(85)90231-7.

[41] D.D. Krueger, S.D. Antolovich, R.H. Van Stone, Effects of grain size and precipitate size on the fatigue crack growth behavior of alloy 718 at 427 °C, Metall. Trans. A. 18 (1987) 1431–1449. https://doi.org/10.1007/BF02646657.

[42] D.T. Ardi, L. Guowei, N. Maharjan, B. Mutiargo, S.H. Leng, R. Srinivasan, Effects of post-processing route on fatigue performance of laser powder bed fusion Inconel 718, Addit. Manuf. 36 (2020) 101442. https://doi.org/10.1016/j.addma.2020.101442.

[43] E. Hosseini, V.A. Popovich, A review of mechanical properties of additively manufactured Inconel 718, Addit. Manuf. 30 (2019) 100877. https://doi.org/10.1016/j.addma.2019.100877.

[44] R.G. Ding, Z.W. Huang, H.Y. Li, I. Mitchell, G. Baxter, P. Bowen, Electron microscopy study of direct laser deposited IN718, Mater. Charact. 106 (2015) 324–337. https://doi.org/10.1016/j.matchar.2015.06.017.

[45] D.T. Ardi, L. Guowei, N. Maharjan, B. Mutiargo, S.H. Leng, R. Srinivasan, Effects of post-processing route on fatigue performance of laser powder bed fusion Inconel 718, Addit. Manuf. 36 (2020) 101442. https://doi.org/10.1016/j.addma.2020.101442.

[46] Y. Ono, T. Yuri, H. Sumiyoshi, E. Takeuchi, S. Matsuoka, T. Ogata, High-Cycle Fatigue Properties at Cryogenic Temperatures in INCONEL 718 Nickel-based Superalloy, Mater. Trans. 45 (2004) 342–345. https://doi.org/10.2320/matertrans.45.342.

[47] T. Denda, P.L. Bretz, J.K. Tien, Inclusion size effect on the fatigue crack propagation mechanism and fracture mechanics of a superalloyDenda, T.H., Bretz, P.L. and Tien, J.K. Metall. Trans. A. 23A 2 (Feb 1992) 519–526, Int. J. Fatigue. 14 (1992) 420–420.

[48] P.R. Bhowal, A.M. Wusatowska-Sarnek, Carbides and Their Influence on Notched Low Cycle Fatigue Behavior of Fine-Grained IN718 Gas Turbine, in: Superalloys 718,

625, 706 Var. Deriv., TMS, 2005: pp. 341–349. https://doi.org/10.7449/2005/Superalloys_2005_341_349.

[49] Z. Song, W. Gao, D. Wang, Z. Wu, M. Yan, L. Huang, X. Zhang, Very-high-cycle fatigue behavior of inconel 718 alloy fabricated by selective laser melting at elevated temperature, Materials (Basel). 14 (2021) 1–16. https://doi.org/10.3390/ma14041001.

[50] L. Zhong, H. Hu, Y. Liang, C. Huang, High cycle fatigue performance of inconel 718 alloys with different strengths at room temperature, Metals (Basel). 9 (2019) 1–14. https://doi.org/10.3390/met9010013.

[51] E. Salvati, A.J.G. Lunt, C.P. Heason, G.J. Baxter, A.M. Korsunsky, An analysis of fatigue failure mechanisms in an additively manufactured and shot peened IN 718 nickel superalloy, Mater. Des. 191 (2020) 108605. https://doi.org/10.1016/j.matdes.2020.108605.

[52] D.B. Witkin, D. Patel, T. V. Albright, G.E. Bean, T. McLouth, Influence of surface conditions and specimen orientation on high cycle fatigue properties of Inconel 718 prepared by laser powder bed fusion, Int. J. Fatigue. 132 (2020) 105392. https://doi.org/10.1016/j.ijfatigue.2019.105392.

[53] C. Jiang, Z.-K. Liu, Computational investigation of constitutional liquation in Al–Cu alloys, Acta Mater. 51 (2003) 4447–4459. https://doi.org/10.1016/S1359-6454(03)00280-5.

[54] B. Radhakrishnan, R.G. Thompson, A phase diagram approach to study liquation cracking in alloy 718, Metall. Trans. A. 22 (1991) 887–902. https://doi.org/10.1007/BF02658999.

[55] N.L. Richards, X. Huang, M.C. Chaturvedi, Heat affected zone cracking in cast inconel 718, Mater. Charact. 28 (1992) 179–187. https://doi.org/https://doi.org/10.1016/1044-5803(92)90080-2.

[56] M. Ni, C. Chen, X. Wang, P. Wang, R. Li, X. Zhang, K. Zhou, Anisotropic tensile behavior of in situ precipitation strengthened Inconel 718 fabricated by additive manufacturing, Mater. Sci. Eng. A. 701 (2017) 344–351. https://doi.org/10.1016/j.msea.2017.06.098.

[57] V.A. Popovich, E. V Borisov, V. Heurtebise, T. Riemslag, A.A. Popovich, V.S. Sufiiarov, Creep and Thermomechanical Fatigue of Functionally Graded Inconel 718 Produced by Additive Manufacturing BT - TMS 2018 147th Annual Meeting & Exhibition Supplemental Proceedings, in: T.M. & Materials Society Metals (Ed.), Springer International Publishing, Cham, 2018: pp. 85–97.

[58] Aerospace Structural Metals Handbook. Volume 4. Non-Ferrous, Heat Resistant Alloys, Air Force, 1972.

[59] Y. Ono, T. Yuri, N. Nagashima, T. Ogata, N. Nagao, Effect of microstructure on high-cycle fatigue properties of Alloy 718 plates, IOP Conf. Ser. Mater. Sci. Eng. 102 (2015). https://doi.org/10.1088/1757-899X/102/1/012001.

[60] Kevinsanny, S. Okazaki, O. Takakuwa, Y. Ogawa, K. Okita, Y. Funakoshi, J. Yamabe, S. Matsuoka, H. Matsunaga, Effect of defects on the fatigue limit of Ni-based superalloy 718 with different grain sizes, Fatigue Fract. Eng. Mater. Struct. 42 (2019) 1203–1213. https://doi.org/10.1111/ffe.12989.

[61] Y. Murakami, Metal fatigue: effects of small defects and nonmetallic inclusions, Academic Press, 2002.

[62] E. Chlebus, K. Gruber, B. Kuźnicka, J. Kurzac, T. Kurzynowski, Effect of heat treatment on the microstructure and mechanical properties of Inconel 718 processed by selective laser melting, Mater. Sci. Eng. A. 639 (2015) 647–655. https://doi.org/https://doi.org/10.1016/j.msea.2015.05.035.

[63] A.R. Balachandramurthi, J. Moverare, N. Dixit, R. Pederson, Influence of defects and as-built surface roughness on fatigue properties of additively manufactured Alloy 718, Mater. Sci. Eng. A. 735 (2018) 463–474. https://doi.org/10.1016/j.msea.2018.08.072.

[64] S. Sui, J. Chen, L. Ma, W. Fan, H. Tan, F. Liu, X. Lin, Microstructures and stress rupture properties of pulse laser repaired Inconel 718 superalloy after different heat treatments, J. Alloys Compd. 770 (2019) 125–135. https://doi.org/10.1016/j.jallcom.2018.08.063.